Geochemistry Geophysics Geosystems G3
AN ELECTRONIC JOURNAL OF THE EARTH SCIENCES
Published by AGU and the Geochemical Society

Article
Volume 8, Number 8
28 August 2007
Q08012, doi:10.1029/2007GC001597
ISSN: 1525-2027

Click Here for Full Article

Rheologic controls on slab dynamics

Magali I. Billen
Department of Geology, University of California Davis, One Shields Avenue, Davis, California 95616, USA (billen@geology.ucdavis.edu)

Greg Hirth
Department of Geology and Geophysics, Woods Hole Oceanographic Institution, Woods Hole, Massachusetts 02543, USA (ghirth@whoi.edu)

[1] Several models have been proposed to relate slab geometry to parameters such as plate velocity or plate age. However, studies on the observed relationships between slab geometry and a wide range of subduction parameters show that there is not a simple global relationship between slab geometry and any one of these other subduction parameters for all subduction zones. Numerical and laboratory models of subduction provide a method to explore the relative importance of different physical processes in determining subduction dynamics. Employing 2-D numerical models with a viscosity structure constrained by laboratory experiments for the deformation of olivine, we show that the observed range in slab dip and the observed trends between slab dip and convergence velocity, subducting plate age, and subduction duration can be reproduced without trench motion (i.e., slab roll-back) for locations away from slab edges. Successful models include a stiff slab that is 100–1000 times more viscous than previous estimates from models of plate bending, the geoid, and global plate motions. We find that slab dip in the upper mantle depends primarily on slab strength and plate boundary coupling, with a small dependence on subducting plate age. Once the slab sinks into the lower mantle the primary processes controlling slab evolution are (1) the ability of the stiff slab to transmit stresses up dip, (2) resistance to slab descent into the higher-viscosity lower mantle, and (3) subduction-induced flow in the mantle-wedge corner.

Components: 13,899 words, 12 figures, 3 tables, 10 animations.

Keywords: subduction; rheology; mantle dynamics; plate tectonics; slab morphology.

Index Terms: 8170 Tectonophysics: Subduction zone processes (1031, 3060, 3613, 8413); 8162 Tectonophysics: Rheology: mantle (8033); 8150 Tectonophysics: Plate boundary: general (3040).

Received 29 January 2007; **Revised** 5 June 2007; **Accepted** 28 June 2007; **Published** 28 August 2007.

Billen, M. I., and G. Hirth (2007), Rheologic controls on slab dynamics, *Geochem. Geophys. Geosyst.*, *8*, Q08012, doi:10.1029/2007GC001597.

1. Introduction

[2] Subducting lithosphere links convection within the Earth's mantle to plate tectonics on the surface, yet how slabs deform in the upper mantle and transmit stresses to shallower depths remains unresolved. Laboratory experiments on the rheology of olivine predict that cold slabs should be strong due to the temperature dependence of the viscosity [*Rubie*, 1984; *Kohlstedt et al.*, 1995]. By contrast several other geophysical constraints are consistent with weak slabs. Global [*Hager*, 1984, 1991; *Zhong and Davies*, 1999] and regional [*Moresi and Gurnis*, 1996; *Billen et al.*, 2003] models of

Copyright 2007 by the American Geophysical Union

the geoid indicate that slabs are less than 100 times more viscous than the surrounding mantle. Models of earthquake depth distribution and orientation of stresses in slabs are also well-matched by slabs that are less than 100 times more viscous than the surrounding mantle [*Vassiliou et al.*, 1984; *Tao and O'Connell*, 1993]. In addition, models of plate bending demonstrate that plate viscosity in the subduction zone must be low to match energy dissipation constraints [*Conrad and Hager*, 1999] and plate motion [*Buffett and Rowley*, 2006]. However, other recent studies show that plate motions are better predicted by models that include slab pull than by models that only include tractions at the base of plates [*Conrad and Lithgow-Bertelloni*, 2002], suggesting that slabs are stiff enough to act as a stress guide to the surface plate. Each of these models provides important constraints on the coupling between mantle convection and plate tectonics. However, they do not constrain whether the inferred slab viscosity is consistent with the dynamic evolution of subducting lithosphere as inferred from the relationship between the shape of slabs and plate kinematics at individual subduction zones.

1.1. Subduction Observables

[3] Sinking of the lithosphere into the mantle is characterized by asymmetric subduction of one plate beneath another with slab dips of 30° to 90°, as constrained by seismicity to depths of 670 km [*Isacks and Barazangi*, 1977] and seismic tomography [*Gudmundsson and Sambridge*, 1998; *Kárason and van der Hilst*, 2001; *Fukao et al.*, 2001]. The relationships between the present-day shape of slabs and slab buoyancy, surface plate motions, seismic coupling and history of subduction provide insight into the physical processes controlling the time evolution of slabs. *Lallemand et al.* [2005] collected a database of subduction-related observations on 159 subduction zone transects, of which 114 are unperturbed by plateau, ridge or seamount subduction and are not at the edge of a slab. This large number of transects facilitates separating the database into subgroups, while still retaining enough profiles in each subgoup to constrain the relationships between plate boundary dip, slab dip and other observations (see *Lallemand et al.* [2005] for details on subgroup definition). The plate boundary dip is defined for depths of 0 to 125 km, while the upper mantle slab dip is defined for 125 to 670 km depth. For example, the subduction zones are divided by maximum slab depth determined by seismicity and seismic tomography. Upper mantle slabs are defined as slabs that do not cross 670 km depth, while lower mantle slabs reach depths greater than 670 km (Figures 1a and 1b).

[4] The statistical treatment by *Lallemand et al.* [2005] confirms some previous conclusions, while challenging others. They find that the average plate boundary dip is 32 ± 9° and slab dip is 58 ± 14°, and that slabs dip more steeply under oceanic overriding plates. In contrast to previous studies they find that slab dip does not correlate with trench polarity, so that an eastward-directed mantle flow [*Garfunkel et al.*, 1986; *Ricard et al.*, 1991] does not appear to have a controlling influence on slab dynamics. Furthermore, they show that while the plate boundary dip is smaller for upper plates that advance toward the trench (i.e., slab roll-back) there is not a strong correlation between slab dip and slab roll-back (Figure 1c). Instead, they show that only 40% of slabs with advancing upper plates (i.e., slab roll-back) have dips that are lower than the mean slab dip, while 79% of slabs with retreating upper plates have dips that are steeper than the mean. Therefore, while they do find a correlation between trench motion and slab dip, there is not a strong correlation between slab roll-back and slab dip. In addition, there is a wide range in slab dip for almost all trench velocities suggesting that some other process has first order effect on slab dip.

[5] The correlation between slab dip and net convergence rate is useful to explore because this relationship can be compared to results from corner-flow models [*Stevenson and Turner*, 1977]. *Lallemand et al.* [2005] show that slab dip does decrease for faster net convergence between the subducting plate and main upper plate (Figure 1d) and they point out that most correlations are better for slabs that cross into the lower mantle. This observation suggests that the deeper portions of the slab are viscously anchored in the lower mantle, which allows the shallow portion of the slab to respond more freely to flow induced by the large-scale surface plate motions.

[6] Several studies conclude that slab dip does not correlate with subducting plate age [*Jarrard*, 1986; *Cruciani et al.*, 2005] (Figure 1e). Furthermore, *Lallemand et al.* [2005] conclude that slab dip does not correlate with any measure of slab buoyancy (i.e., slab pull force, thermal parameter). These observations are somewhat paradoxical, as subduction is driven by slab buoyancy and therefore there is an expectation that variations in plate age should

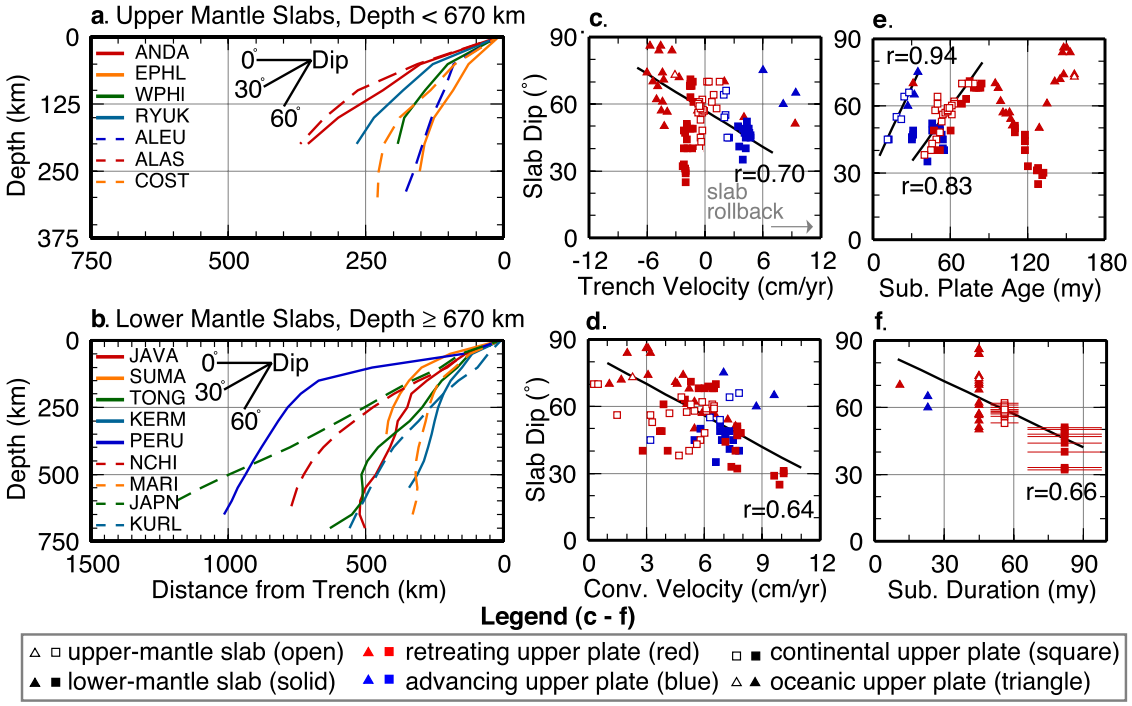

Figure 1. Slab shape and subduction zone observations. (a and b) Profiles of slab shape [*Gudmundsson and Sambridge*, 1998] separated by maximum slab depth as defined by *Lallemand et al.* [2005]: upper mantle slabs (z_{slab} < 670 km) and lower mantle slabs ($z_{slab} \geq$ 670 km). (c–e) Slab dip dependence on trench motion, convergence velocity, and subducting plate age. Subduction zone observations are from *Lallemand et al.* [2005]; velocity is positive toward the trench and trench-normal. Note that symbol types are combined to denote subgroups; for example, open red squares denote profiles with upper mantle slabs subducting beneath retreating, continental upper plates. Line fits for trench velocity and convergence velocity are for lower mantle slabs only (solid symbols) and are the same as found by *Lallemand et al.* [2005]. Line fits for subducting plate age are for upper mantle slabs with continental overriding plates only (square, open symbols) with separate fits for slabs with retreating and advancing upper plates. *Lallemand et al.* [2005] concluded there was no correlation of slab dip with subducting plate age. (f) Slab dip versus subduction duration with data from *Jarrard* [1986] and *Gurnis et al.* [2004].

have a direct affect on slab dip. However, there does appear to be a positive correlation between slab dip and slab age for upper mantle slabs younger than 90 Ma, with separate trends for advancing and retreating overriding plates (Figure 1e). These trends for upper mantle slabs suggests that the effect of plate age may be obscured by other processes once the slab starts to interact with the lower mantle. Finally, these data also support a previous observation that slab dip decreases with longer durations of subduction (Figure 1e) [*Gurnis and Hager*, 1988; *Gurnis et al.*, 2004].

[7] In summary, while several trends and correlations emerge from these data, determining under what circumstances individual processes dominate remains challenging. We present numerical simulations that explore the influence of mantle rheology on the evolution of slab shape, and use the predicted correlations among subduction observables to determine the processes that produce the observed relationships. Coupled with dynamical models, in which individual correlations can be investigated while keeping other parameters fixed, this large data set provides important constraints on the physical processes controlling slab dynamics in the upper mantle and illustrates some of the limitations of previous subduction models.

1.2. Subduction Models

[8] Our understanding of subduction dynamics has developed from two main classes of models: (1) those with perfectly rigid slabs typically used in corner flow models to study the steady-state balance of forces on slabs and (2) those with viscous slabs employed in numerical and laboratory flow models. The corner flow model of subduction defined by a rigid slab of fixed length, subduction velocity and uniform dip [*McKenzie*, 1969] pre-

dicts a steady-state slab dip of ~54–63° assuming non-Newtonian [*Tovish et al.*, 1978] or Newtonian [*Stevenson and Turner*, 1977] mantle viscosity. Despite the obvious limitation of this model that the slab cannot deform, these estimates agree well with the mean dip of slabs (i.e., 58° [*Lallemand et al.*, 2005]) and the model correctly predicts that slab dip decreases for higher convergence rates (Figure 1d). However, contrary to observations (Figures 1a–1c) the rigid-slab model also predicts that (1) slab dip should correlate strongly with slab buoyancy because the slab dip is determined by a balance between slab buoyancy and stresses on the slab due to surrounding mantle flow and (2) a slab dipping less than ~40° will be unstable due to the suction forces created by flow in the wedge corner, which causes the slab to shallow until it is flat beneath the upper plate. By contrast, slab dip at depths of 0 to 200 km are commonly ~30° (Figures 1a and 1b). The use of rigid slabs also prevents analysis of the implications of energy dissipation within the slab [*Tovish et al.*, 1978; *Conrad and Hager*, 1999] and the feedbacks between slab temperature (age) and both slab density and slab viscosity [*Kemp*, 1992; *Royden and Husson*, 2006].

[9] Time-dependent viscous flow models of slab evolution illustrate the interplay of trench migration, slab strength, and the mantle viscosity and density structure. One of the first models of viscous slabs demonstrated that relatively weak slabs (η_{slab}/η_o = 500) fold and thicken upon entry into a higher-viscosity lower mantle and that slab dip decreased in response to slab rollback [*Gurnis and Hager*, 1988]. Subsequent numerical models show that the combination of rapid trench retreat and a large density contrast for the spinel-to-perovskite phase change (670 km) can "trap" weak slabs in the transition zone [*Christensen*, 1996; *Tetzlaff and Schmeling*, 2000]. In addition, recent laboratory models show that when the slab is prevented from entering the lower mantle, subduction with either retreating or advancing trenches occurs for a range of subduction velocities [*Bellahsen et al.*, 2005].

[10] However, it is more difficult to prevent stronger slabs ($\eta_{slab}/\eta_o = 10^4$–$10^6$) from sinking directly into the lower mantle. Even when processes that weaken slabs are included, such as grain-size reduction related to the olivine-spinel phase change, trench retreat rates of more than 4 cm/yr are needed to trap slabs in the transition zone [*Cížková et al.*, 2002]. These models show that depending on (1) the magnitude of the viscosity jump or clapeyron slope for the phase changes, (2) the rate of trench migration, and (3) the strength of the slab, the slab can either cross unperturbed into the lower mantle, form temporary piles, or lie flat in the transition zone. All three of these slab morphologies are inferred from seismic tomography [e.g., *Fukao et al.*, 2001; *Kárason and van der Hilst*, 2001].

[11] Slab evolution in the absence of trench motion has received less attention, in part because the weak slabs typically used in numerical models sink vertically into the mantle and easily enter the lower mantle even in the presence of viscosity jumps and phase changes [*Christensen*, 1996; *Kincaid and Sacks*, 1997; *King*, 2001]. Such models with uniformly weak slabs are incapable of reproducing the observed range in slab dip or shallow dips (30–40°) at depths of 100–400 km. Models with stronger slabs and slow slab rollback (1 cm/yr) do have shallower slab dips [*Cížková et al.*, 2002]. In addition, 3-D models show that roll-back rate depends on the length of the subduction zone, with short subduction zones exhibiting fast roll-back, while the central regions of long subduction zones are stationary [*Schellart et al.*, 2007]. Together with previous 3-D laboratory models [e.g., *Funiciello et al.*, 2003; *Bellahsen et al.*, 2005; *Piromallo et al.*, 2006], *Schellart et al.* [2007] demonstrate the importance of toroidal flow for slab dynamics near slab edges.

[12] To complement many of the recent models that focused on the effects of trench motion on slab dynamics, we focus on what controls slab evolution in the absence of trench motion. We use 2-D numerical models of subduction to determine how the behavior of stiff slabs depends on mantle viscosity structure. In particular, we constrain the slab stiffness required to reproduce the observed correlations among subduction observables (slab dip, convergence velocity and subducting plate age). We focus on the long-term (>50 my) evolution of slabs. Because previous models have shown that the phase changes do not have a strong effect on slabs without trench motion, we do not include the effects of phase changes in the models presented here.

2. Rheology of the Mantle and Subducting Slabs

[13] The fact that the two classes of subduction models explain different aspects of the subduction-

related observations suggest that slabs must be deformable, yet stiff enough to maintain shallow slab dips over long periods of time. A combination of experimental and theoretical constraints indicate that at shallow depths the cold crust and lithosphere deform by brittle processes in accordance with Mohr-Coulomb failure criteria [*Kohlstedt et al.*, 1995]. As pressure increases but temperature remains relatively low in the lithosphere, brittle deformation gives way to ductile deformation, in which the material strength is controlled by low-temperature plasticity [*Goetze and Evans*, 1979; *Hirth*, 2003]. In addition, the rheology of the lithospheric mantle is stratified owing to differences in water content that results from the melting processes at mid-ocean ridges [*Braun et al.*, 2000]. Beneath the lithosphere, as temperature increases with depth, thermally activated deformation mechanisms such as diffusion creep (Newtonian viscosity) and dislocation creep (non-Newtonian, stress-dependent viscosity) accommodate deformation [*Karato and Wu*, 1993; *Karato and Jung*, 2003; *Hirth and Kohlstedt*, 2003].

[14] Like the lithosphere near the Earth's surface, the strength of the cold slab at higher pressure in the mantle depends on the ductile yield strength. In this study we focus on the effects of temperature-dependent and non-Newtonian viscosity and the slab yield strength. Variations in composition, melt content, and grain size also affect rheology, but are not included in these models. However, the effect of a dry versus a wet slab is considered. In analyzing the results of our models we draw on the conclusions of other studies that have explored model parameters that we have not included [e.g., *Christensen*, 1996; *van Hunen et al.*, 2001; *Cížková et al.*, 2002]. The range in viscosity variation, rheology and slab stiffness used in the models presented here is similar to that used in several previous studies of subduction dynamics [*Schmeling et al.*, 1999; *Karato et al.*, 2001; *Cížková et al.*, 2002].

2.1. Upper Mantle Viscosity

[15] The dynamics of the slab depend on the slab stiffness relative to the viscosity in the surrounding mantle. In the upper mantle, deformation is accommodated by both diffusion (df) and dislocation (ds) creep, with each mechanism accommodating part of the total strain rate,

$$\dot{\epsilon} = \dot{\epsilon}_{df} + \dot{\epsilon}_{ds} \tag{1}$$

For deformation at constant stress, the composite viscosity in the mantle is given by

$$\eta_{comp} = \frac{\eta_{df}\eta_{ds}}{\eta_{df} + \eta_{ds}} \tag{2}$$

where η_{df} and η_{ds} are the diffusion and dislocation creep viscosity for olivine. The general form of the viscosity law, assuming constant stress is given by

$$\eta_{df,ds} = \left(\frac{d^p}{AC_{OH}^r}\right)^{\frac{1}{n}} \dot{\epsilon}_{II}^{\frac{1-n}{n}} \exp\left[\frac{E + P_{lc}V}{nRT_t}\right] \tag{3}$$

where $\dot{\epsilon}_{II}$ is the second invariant of the strain-rate tensor, P_{lc} is the lithostatic pressure, including a compressibility gradient in the mantle, and $T_t = T + m_{ad}z$ is the total temperature (T is the temperature due to convective flow defined by equation (7), m_{ad} is the adiabatic temperature gradient (0.3 K/km) and z is depth). The viscous flow law parameters for olivine, defined and listed in Table 1, give a background viscosity of $\eta_o = 10^{20}$ Pas at a depth of 250 km and transition strain rate of $\dot{\epsilon}_t = 10^{-15}$ s^{-1} (i.e., $\dot{\epsilon}_{df} = \dot{\epsilon}_{ds}$) in agreement with estimates of upper mantle viscosity from post-glacial rebound and plate velocity models [e.g., *Hager*, 1991]. The water content of the mantle olivine (C_{OH} = 1000 ppm-H/Si) and grain size are chosen to fix the absolute magnitude of viscosity and the transition strain rate. For strain rates larger than the transition strain rate, the effective viscosity is dominated by the dislocation creep mechanism and decreases with increasing strain rate, while at lower strain rates diffusion creep controls the effective viscosity (Figure 2a).

2.2. Slab Strength

[16] Laboratory experiments on the deformation of olivine indicate that slabs should be stiff due to the strong temperature dependence of viscosity. For example, the predicted viscosity of a slab with a temperature of ~800°C at a depth of 400 km is $\sim 10^{26}$–10^{27} Pas for deformation by diffusion creep (d = 10 mm, C_{OH} = 1000 ppm-H/Si). For a strain rate of 10^{-15}–10^{-16} s^{-1} the corresponding stress in the slab would be 10–1000 GPa (Figure 2b) far exceeding the yield stress of the rock predicted by low-temperature plasticity (~1–2 GPa). In addition, taking into account the difference in water content of the slab (C_{OH} = 1–10 ppm-H/Si) the slab viscosity and predicted strength are ~100 times larger. Therefore we employ a constant

Table 1. Viscous Flow Law Parameters[a]

	Parameter	Diffusion	Dislocation
n	stress exponent	1.0	3.5
A	preexponential factor[b]	1.0	90×10^{-21}
E	activation energy, kJ/mol	335	480
V	activation volume, m^3/mol		
	upper mantle	4.0×10^{-6}	11.0×10^{-6}
	lower mantle	1.5×10^{-6}	–
d	grain size, μm		
	upper mantle ($\dot{\epsilon}_t = 10^{-15}$ s^{-1})	10.0×10^3	
	lower mantle, $\eta_{lm/um} = 1$	40.0×10^3	–
	lower mantle, $\eta_{lm/um} = 10$	73.5×10^3	–
	lower mantle, $\eta_{lm/um} = 30$	105.4×10^3	–
p	grain-size exponent	3.0	–
$\mathbf{C_{OH}}$	OH concentration, ppm-H/Si (mantle/slab)	1000/1	1000/1
r	C_{OH} exponent	1.0	1.2
	Yielding		
σ_y	yield stress, MPA	1000, 500, or 100	

[a] Model rheology. Parameters for viscous flow of wet olivine at constant water content from *Hirth and Kohlstedt* [2003] (used in equation (3)). Values for the lower mantle are the same as those for diffusion creep in the upper mantle, except for the parameters listed, which are chosen to reproduce an approximately constant viscosity and the prescribed viscosity jump at the upper-lower mantle boundary ($\eta_{lm/um}$). The higher-viscosity lower mantle is modeled as deforming by diffusion creep with a larger grain size.
[b] The value of A is given for stress in Pa, d in μm, C_{OH} in ppm-H/Si and the stress exponents listed.

yield stress, σ_y, which limits the strength of slab such that the maximum effective viscosity is

$$\eta_{ef} = \min\left(\frac{\sigma_y}{\dot{\epsilon}_{II}}, \eta_{comp}\right) \quad (4)$$

In this formulation, once the yield stress is reached all the deformation is accommodated by plastic deformation, rather than assuming that some portion of the strain is also accommodated by power-law creep [*van den Berg et al.*, 1993; *Cížková et al.*, 2002]. The effect of the yield stress is to locally decrease the effective viscosity of the slab in regions of rapid deformation. In most models the yield stress is 1000 MPa, similar to the stress predicted for low-temperature plasticity at

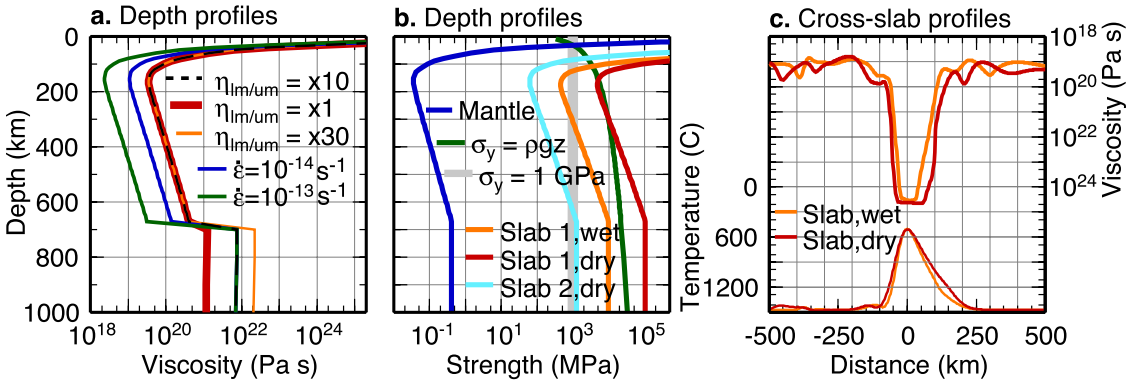

Figure 2. Effective viscosity and yield strength. (a) Viscosity depth profiles, at a strain rate of 10^{-15} s^{-1} (unless noted), for the reference model (black-dashed, $\eta_{lm/um} = 10$) and models with smaller (red, $\eta_{lm/um} = 1$) or larger (orange, $\eta_{lm/um} = 30$) lower mantle viscosity. Higher strain rates (blue and green) decrease the upper mantle viscosity and will locally increase the actual jump in viscosity from the upper to lower mantle. (b) Viscous stress in the mantle at a strain rate of 10^{-15} s^{-1} and for three slab profiles. Slab 1, wet (orange): $C_{OH} = 1000$ ppm-H/Si, $\dot{\epsilon} = 10^{-15}$ s^{-1}, $T_{slab} = T_{mantle} - 500$. Slab 1, dry (red): $C_{OH} = 1$ ppm-H/Si, $\dot{\epsilon} = 10^{-15}$ s^{-1}, $T_{slab} = T_{mantle} - 500$. Slab 2, dry (cyan): $C_{OH} = 1$ ppm-H/Si, $\dot{\epsilon} = 10^{-16}$ s^{-1}, $T_{slab} = T_{mantle} - 800$. Goetze's yield criterion (green) is applicable at shallow depths with values reaching 1000 MPa at ~100 km depth. A constant yield stress of 1000 MPa (gray) is used in this study unless otherwise noted.

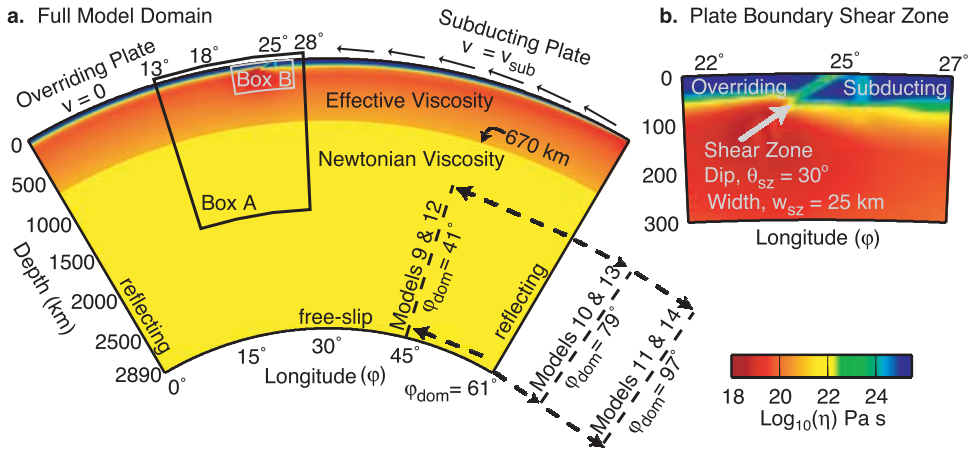

Figure 3. Initial and boundary conditions. (a) Full domain for models with a width of $\phi_{dom} = 61°$ (models 1–8) is shown with the initial viscosity structure in color. The domain width for models 9–14 is decreased or increased by moving the right-side model boundary ($\phi_{dom} = 41°$, 79°, or 97°). The overriding plate extends from $\phi = 0$–25° with a 30° dipping shear zone at $\phi = 25°$ in all models. Box A indicates the region of the model shown in subsequent figures ($\phi = 13$–28°, 0–1500 km). Box B indicates the region surrounding the shear zone ($\phi = 21$–27°, 0–300 km). (b) Zoom-in of region in Box B showing low-viscosity shear zone between the subducting and overriding plates.

600–700° [*Goetze and Evans*, 1979]. In addition, the effect of a smaller yield strength (100 MPa and 500 MPa) is used to explore the possible influence of other slab weakening processes such as grain-size reduction.

2.3. Plate Boundary Shear Zone

[17] The boundary between the overriding and subducting plate can be modeled as either a discrete fault [*Zhong and Gurnis*, 1986; *Kincaid and Sacks*, 1997; *Billen et al.*, 2003] or as a narrow low-viscosity shear zone [*Kukaèka and Matyska*, 2004; *Billen and Hirth*, 2005]. The drawback of using a fault is the presence of a stress discontinuity at either end of the fault. The stress singularity in the mantle can be avoided by tapering the degree of coupling along the fault [*Toth and Gurnis*, 1998; *van Hunen et al.*, 2000], but the discontinuity at the surface leads to inaccurate topography. In low-resolution models, using a discrete fault is preferable to a broad low-viscosity region, which is not capable of fully decoupling the two plates [*Zhong et al.*, 1998]. However, in higher-resolution models (element width <5 km) a narrow low-viscosity shear zone effectively decouples the two plates and there is no stress discontinuity.

[18] We model the plate boundary as a 25 km wide (10 elements), low-viscosity region dipping at 30°. Observed plate boundary dips increase from 2–10° at the surface to an average of 32 ± 9° for depths of 0–125 km [*Lallemand et al.*, 2005]; therefore the dip angle in the models represents the average dip of most subduction zones. The viscosity of the shear zone is either equal to, or is ten times, the background mantle viscosity ($\eta_{sz} = 10^{20}$ or 10^{21} Pas). We use a constant viscosity for the shear zone (no depth dependence), which is consistent with the trade-off between an increase in water content with depth and the activation volume term in a water-saturated layer above the slab [*Hirth and Kohlstedt*, 2003].

2.4. Lower Mantle Viscosity

[19] The viscosity of the lower mantle, composed of rocks with primarily perovskite mineralogy, is not well constrained by laboratory measurements, but is estimated to be 10–100 times that in the upper mantle based on geophysical constraints [*Hager*, 1991] and may dominantly deform by diffusion creep as inferred by the limited observations of seismic anisotropy in the lower mantle [*Kendall*, 2000; *Ritsema*, 2000]. Therefore we use the same diffusion creep flow law as that used in the upper mantle, but modify the activation volume and grain size to create a uniform viscosity with depth and control the viscosity jump at 670 km (Table 1 and Figure 2a). As in the upper mantle, the viscosity of the cold interior of the slab is limited by the yield stress.

3. Methods

[20] The subduction models are dynamic, two-dimensional, mantle convection simulations, which

Table 2. Fixed Model Parameters[a]

	Parameter	Value
	Dimensionalization	
ρ_o	reference density, kg/m^3	3300
α	thermal expansion coefficient, K^{-1}	2.0×10^{-5}
ΔT	temperature change across lithosphere, K	1400
g	gravitational acceleration, m/s^2	9.81
R	Earth radius,[b] km	6371
κ	thermal diffusivity, m^2/s	10^{-6}
η_o	reference viscosity, Pas	10^{20}
Ra	Rayleigh number	2.34×10^9
	Geometry	
A_{up}	upper plate age, my	40
θ_{sz}	shear zone dip, deg	30
w_{sz}	shear zone width, km	25
z_{cmb}	model domain depth, km	2890
$z_{lm/um}$	upper-lower mantle boundary depth, km	670

[a] Model dimensionalization and geometry. The parameters listed here are kept constant in all models. Parameters that are varied are listed in Table 3.

[b] The reference length-scale for the Rayleigh number in the spherical-geometry, finite-element model CitcomT is defined as the Earth's radius, not the depth of the convecting layer.

incorporate the viscosity structure described above and boundary conditions to control the rate of subduction (Figure 3a). We solve the standard equations of conservation of mass, momentum and energy, without internal heating for flow in an incompressible viscous fluid in which inertial forces are negligible,

$$\nabla \cdot \mathbf{u} = 0 \tag{5}$$

$$\nabla \cdot \sigma + \mathbf{f} = 0 \tag{6}$$

$$\dot{T} = -\mathbf{u} \cdot \nabla T + \kappa \nabla^2 T \tag{7}$$

where $\mathbf{u}$ is the velocity, $\mathbf{f} = \rho_o \alpha (T - T_o) g \delta_{rr}$ is the force due to density variations related to temperature (T_o = 1673 K), and $\sigma_{ij} = -P\delta_{ij} + \eta_{ef}\dot{\epsilon}_{ij}$ is the stress tensor defining the constitutive relation. The pressure, P, is defined as the second invariant of the stress tensor, and can be expressed as the sum of the lithostatic pressure, P_l (without compressibility), and the dynamic pressure, P_{dyn}, resulting from viscous flow (i.e., $P = P_l + P_{dyn}$). The equations are solved using the spherical-geometry finite-element code, CitcomT [*Zhong et al.*, 1998; *Billen et al.*, 2003]. The dimensional parameters used in the Rayleigh number and the geometry are given in Table 2.

3.1. Model Setup

[21] The model domain is a 2-D slice through a sphere taken at the equator and extends 2890 km from the surface to the core-mantle boundary (Figure 3a). Because the model is a slice through a 3-D spherical model, it actually represents a slab subducting along a small circle and preserves the proper 3-D spherical volume changes with depth. The bottom boundary is isothermal (T = 1673 K) and is a free-slip boundary (i.e., flow must become tangent to the boundary). The model surface is divided into an overriding plate, which is immobile at the surface and a subducting plate with a fixed subduction velocity, v_{sub}. The plate boundary is modeled as a dipping, low-viscosity shear zone as described in the previous section (Figure 3b). The mesh element size varies from 2.5 km, in a 1000 km wide section centered on the plate boundary, to 15 km at the sides of the model domain, and 2.5 km, in the top 150 km of the mesh, to 10 km in the lower mantle. At the start of the simulation, passive tracer particles are placed at a depth of 1 km along the full length of the subducting plate. These tracer particles are advected and track the slab surface in the mantle.

[22] In all models the overriding plate extends 25° in longitude (ϕ = 0–25°). The thermal structure of the plate directly above the slab is most important for the slab evolution. While the age of overriding plates varies significantly, the island arc region is thought to have temperatures of 1200–1400°C at depths of 50 km due in part to convective erosion from melt and volatile weakening of the overriding lithosphere [*Kelemen et al.*, 2003; *Arcay et al.*, 2007; A.-M. Cagnioncle et al., The effect of solid flow above a subducting slab on water distribution and melting at convergent plate boundaries, submitted to *Journal of Geophysical Research*, 2007]. Therefore a warm and thin overriding plate is appropriate and it is assigned an initial thermal structure determined by a half-space cooling model for a 40 my old plate.

[23] To facilitate study of the influence of subducting plate age and subduction velocity independently, the width of the subducting plate was varied in subsets of models by increasing the width of the model domain. In models 1–8, the subducting plate extends from ϕ = 25–61°. The age of the subducting plate varies from 0 my at the model domain boundary (ϕ = 61°) to 80 my at the plate

Table 3. Model Parameters and Results[a]

	Parameters Varied						Results Summary					
	v_{sub}, cm/yr	A_{sub}, my	ϕ_{dom}	$\frac{\eta_{lm}}{\eta_{um}}$	$\frac{\eta_{sz}}{\eta_o}$	σ_y, MPa	$\lvert\alpha_i\rvert$	$\lvert\alpha_d\rvert$	v_{h670}, cm/yr	Sub. Type	t_{st}, my	Animation
1	5.0	80	61°	10	10	1000	48 ± 8°	63 ± 12°	−0.7	M	>89	1
1ws	5.0	80	61°	10	10	1000	62 ± 11°	76 ± 15°	−0.9	M	>78	–
2	5.0	80	61°	**30**	10	1000	36 ± 12°	50 ± 21°	−1.0	NS	>100	3
3	5.0	80	61°	**1**	10	1000	78 ± 9°	95 ± 9°	−0.1	S	>53	4
4	5.0	80	61°	10	**1**	1000	60 ± 17°	74 ± 25°	−2.5	M	>72	–
5	5.0	80	61°	**30**	**1**	1000	40 ± 25°	54 ± 38°	−1.8	NS	>98	5
6	5.0	80	61°	**1**	**1**	1000	92 ± 12°	98 ± 29°	−0.2	S	>63	6
7	5.0	80	61°	10	10	**500**	64 ± 7°	81 ± 8°	−0.6	S	>39	–
8	5.0	80	61°	10	10	**100**	91 ± 25°	NA	NA	NS	NA	2
9	5.0	**40**	**43°**	10	10	1000	52 ± 8°	71 ± 5°	−0.7	M	>87	7
10	5.0	**120**	**79°**	10	10	1000	53 ± 9°	69 ± 7°	−1.0	NS	>72	8
11	5.0	**160**	**97°**	10	10	1000	56 ± 9°	71 ± 8°	−1.9	NS	>74	–
12	**2.5**	80	**43°**	10	10	1000	60 ± 4°	79 ± 7°	−0.7	S	>92	9
13	**7.5**	80	**79°**	10	10	1000	45 ± 8°	59 ± 12°	−1.0	NS	>60	–
14	**10.0**	80	**97°**	10	10	1000	35 ± 8°	45 ± 12°	−1.0	NS	>72	10

[a] Parameters that differ from the reference model (Model 1: also see Tables 1 and 2) are in bold text: v_{sub}, convergence velocity; A_{sub}, subducting plate age; ϕ_{dom}, domain width; $\eta_{lm/um}$, lower-to-upper mantle viscosity ratio; η_{sz}/η_o, ratio of shear zone viscosity to reference viscosity; $|\alpha_i|$, intermediate depth dip (z = 200–400 km); $|\alpha_d|$, deep dip (z = 400–670 km), v_{h670}, lateral migration rate of slab at 670 km; subduction type (S, steady state; NS, non–steady state; M, mix mode); and t_{st}, duration of stable subduction. NA indicates that the measurement is not applicable to the model dynamics. All models have C_{OH} = 1 ppm-H/Si in the lithosphere and slab ($T \leq 900°$), except model 1ws (ws, wet slab), which has C_{OH} = 1000 ppm-H/Si. For models with $\eta_{lm/um}$ = 10, the actual jump is ∼13–30 ($\eta_{lm} \approx 8 \times 10^{21}$ Pas, $\eta_{um} \approx 8 \times 10^{19}$ Pas). For models with $\eta_{lm/um}$ = 1, the actual jump is ∼3–4 ($\eta_{lm} \approx 1.5 \times 10^{21}$ Pas, $\eta_{um} \approx 6 \times 10^{19}$ Pas). For models with $\eta_{lm/um}$ = 30, the actual jump is ∼39–54 ($\eta_{lm} \approx 2.3 \times 10^{22}$ Pas, $\eta_{um} \approx 1.1 \times 10^{20}$ Pas).

boundary shear zone (ϕ = 25°), and the initial thermal structure is determined by a half-space cooling model. The width of the model domain was chosen such that at a constant subduction velocity (v_{sub} = 5.0 cm/yr) the age of the subducting plate at the plate boundary is constant (80 my). In models 9–11 the width of the subducting plate is varied to control the plate age, A_{sub}, at a fixed subduction velocity (5.0 cm/yr), while in models 12–14 the width of the subducting plate is varied to keep the plate age constant (80 my), while varying the subduction velocity (Figure 3a and Table 3). While the age of the subducting plate at real subduction zones varies with time, designing the models with a constant subducting plate age allows us to analyze the effect of plate age on subduction dynamics without other complications.

3.2. Boundary Conditions

[24] The boundary conditions on the top and sides of the model domain were chosen to minimize their influence on the evolution of the slab in the mantle, while facilitating the study of slab evolution in the absence of trench motion. The sides of the model domain are modeled as reflecting (free-slip) boundaries, which explicitly creates a reference frame for motion that is fixed with respect to model domain. The minimum width of the overriding and subducting plates were chosen in conjunction with the depth of the model domain to insure that the subducting slab is not affected by the side boundaries (see discussion in Appendix A).

[25] Prescribed velocity boundary conditions on the surface of the model are used to initiate subduction and to control the subducting plate velocity and/or subducting plate age. We have calculated the work done by the kinematic boundary conditions on the subducting plate and underlying mantle and compared this to the work done by the subducting slab on the surrounding mantle (see Appendix A for calculation and discussion). We find that after the initiation of subduction the work done by the slab on the mantle is 25 to 300 times the work done by the kinematic boundary conditions for all models presented here. Therefore, in agreement with previous results for weak to moderately strong slabs [*Han and Gurnis*, 1999], the evolution of the slab in the mantle is not controlled by the kinematic boundary conditions.

4. Results

[26] We evaluate the dynamics of subduction, in the absence of trench motion, by systematically

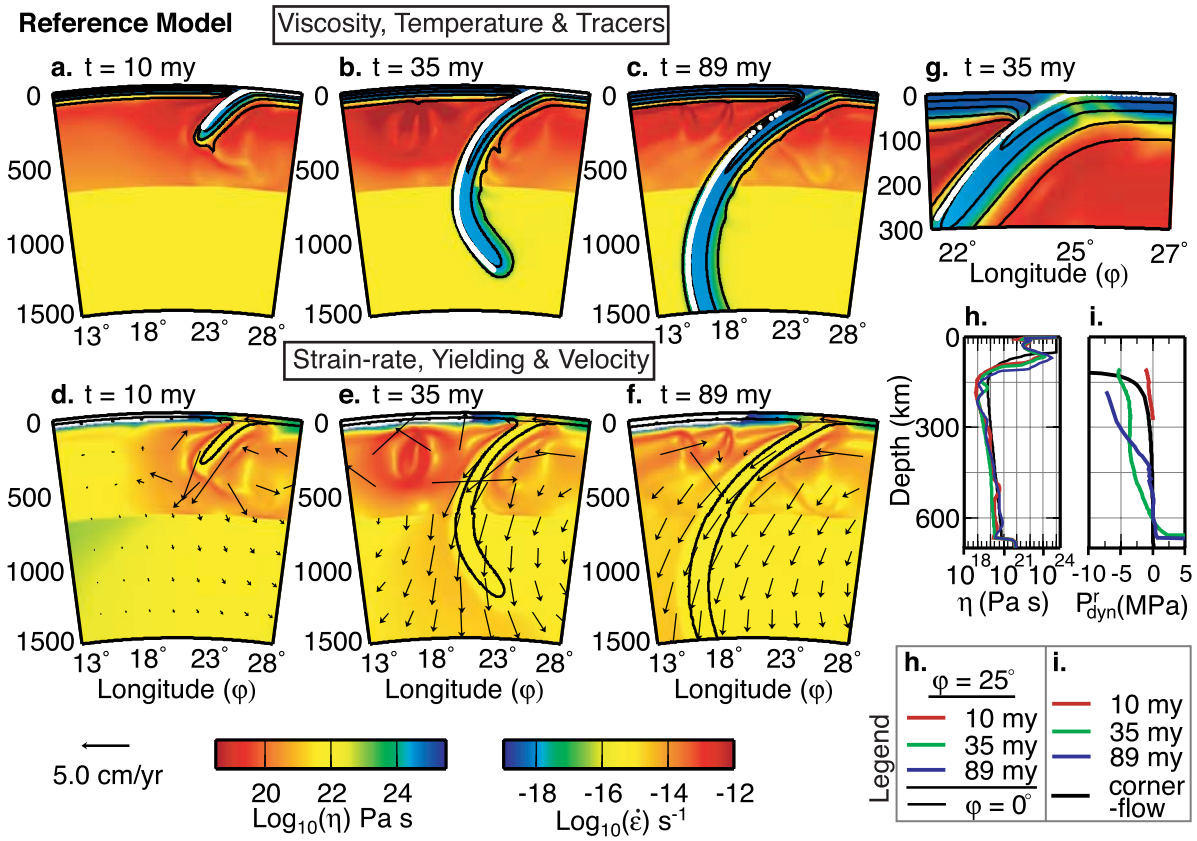

Figure 4. Reference model results. (a–c) Viscosity (color), temperature (black contours every 300°C), and tracer particles on the slab surface (white dots, 1 km initial depth) for three times: 10 my, 35 my, and 89 my. (d–f) Strain rate (color), yielding region (inside black contour), and velocity field for the same times. Note that only the region in Box A from Figure 3 is shown. (g) Zoom-in on plate boundary region (Box B, Figure 3) showing tracers on top of the subducting slab and local region of bending-induced yielding in the subducting plate. (h) Radial viscosity profiles at $\phi = 0°$ for $t = 10$ my and $\phi = 25°$ (behind slab) for three times showing local variation in viscosity due to stress-dependent rheology. (i) Slab surface profiles of dynamic pressure, relative to the value at 600 km depth, are similar to that expected for slab-induced corner flow in the wedge (black). Profiles are located ~25 km above the slab surface (as defined by the tracers).

varying the viscosity structure and subduction parameters with respect to a reference model (model 1; see Table 3). We present the results in three parts. First, we discuss the reference model in detail, describing the slab evolution and how aspects of the rheology and resulting flow affect the slab dynamics. Second, we present models with different rheological structures to illustrate the effects of a dry versus wet slab, the yield stress, the upper-lower-mantle (ULM) viscosity contrast and the plate boundary coupling (shear zone viscosity). Third, we present the results of varying the subducting plate velocity or age, for our preferred rheologic model, and compare the model systematics to the subduction observations presented in the introduction. The model results are presented in Figures 4–9 and Table 3. Animations showing the time-dependent evolution of the slabs are also included for a subset of models (Animations 1–10[1]).

4.1. Reference Model

[27] The reference model (model 1) includes a stiff slab (σ_y = 1000 MPa, $C_{OH}(slab)$ = 1 ppm-H/Si), a moderate viscosity increase into the lower mantle (×10) and a "coupled" shear zone (η_{sz}/η_o = 10). The subducting plate velocity is 5 cm/yr and the subducting plate age at the trench is 80 my. The slab evolution starts out with a shallow dipping slab (<40°) that gradually steepens in responses to the growing negative slab buoyancy, until the slab reaches the ULM boundary (Figures 4a and 4d and Animation 1). A region of high strain rate surrounds

[1] Animations 1–10 are available in the HTML.

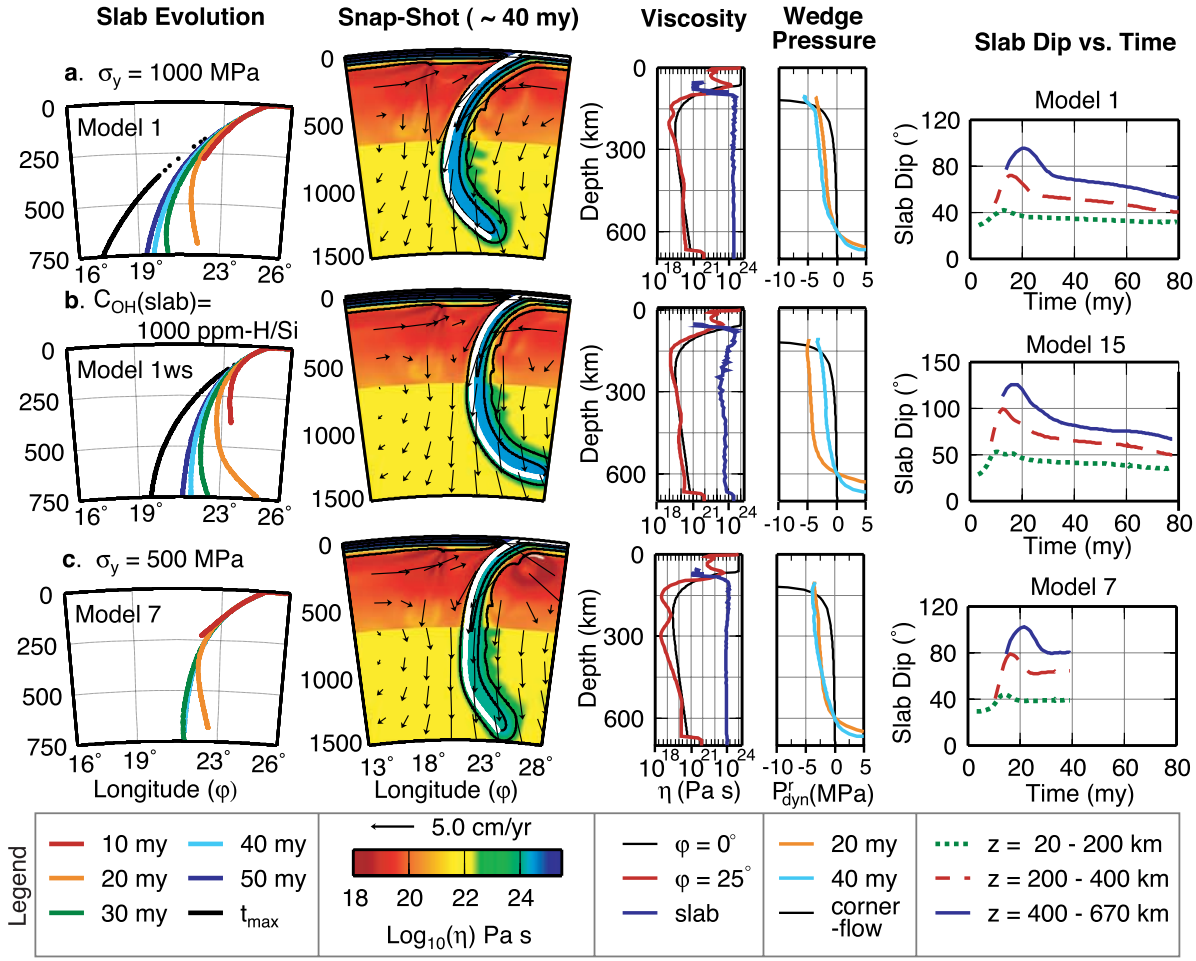

Figure 5. Slab evolution dependence on slab strength. (a) Reference model results (model 1) with σ_y = 1000 MPa, showing the slab shape at six times (column 1), a snapshot at ~40 my (column 2), viscosity profiles (column 3), slab surface profiles of dynamic pressure (column 4), and slab dip as a function of time for three depth intervals (column 5). The legend defines the curves for each subfigure. (b) Same as Figure 5a but for model 1ws with a wet slab (C_{OH} = 1000 ppm-H/Si). (c) Same as Figure 5a but for model 7 with a yield stress of σ_y = 500 MPa.

the slab that, owing to the non-Newtonian rheology of the upper mantle, significantly decreases the viscous resistance to the slab sinking in the upper mantle. High strain rates in the mantle wedge above the slab also create a low-viscosity region that keeps the slab decoupled from the overriding plate beyond the tip of the shear zone [see also *Billen and Hirth*, 2005]. The strain rate within the slab, $\sim 10^{-15}$–10^{-16} s^{-1}, is consistent with minimum estimates based on seismic moment release at depths of 75–175 km [*Bevis*, 1988].

[28] Once the slab crosses into the lower mantle, the average dip in the upper mantle decreases as the slab migrates toward the overriding plate (Figures 4b and 4c). This lateral migration occurs in response to the increase in viscous resistance on the slab in the higher-viscosity, Newtonian lower mantle. Because the slab is stiff, it transmits stresses to the upper mantle portion of the slab, which migrates laterally to accommodate the difference in sinking rates in the two layers. The large-scale flow follows the sinking slab into the deep lower mantle, while a corner flow develops in the mantle wedge corner above the slab (Figures 4e and 4f).

[29] The slab interior remains cold ($T < 900°$) and deforms at relatively high stress to depths of almost 1500 km after 50 my of subduction (black contours in Figures 4d–4f). The transition from viscous deformation to deformation by plastic yielding occurs at temperatures of 700–850°C. In the shallow mantle, the yielding behavior leads to a region of bending-induced weakening in the outer rise of the subducting plate (Figure 4g). The viscosity in

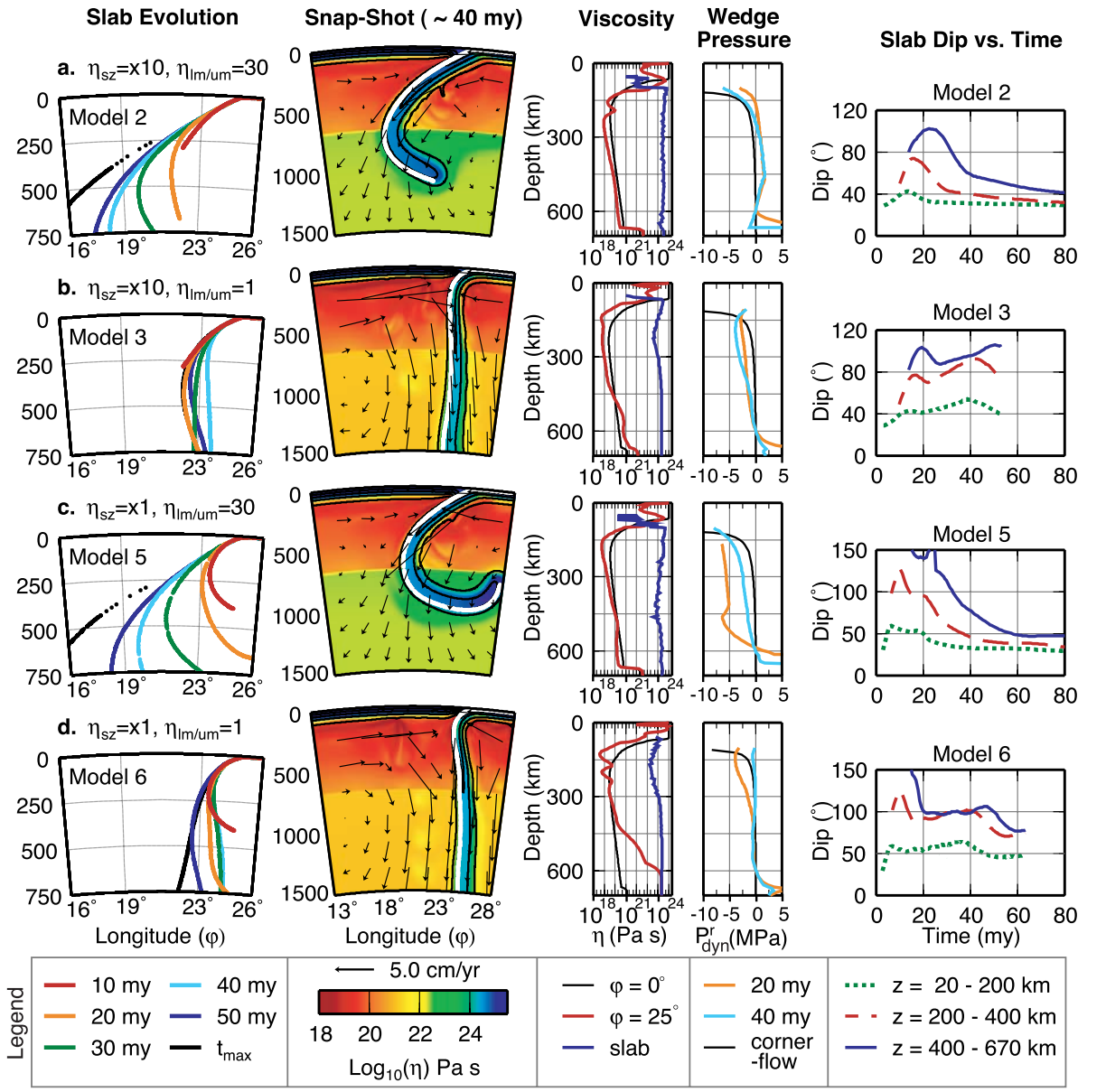

Figure 6. Slab evolution dependence on mantle viscosity structure. (a and b) Coupled shear zone models (η_{sz}/η_o = 10) with a higher-viscosity (model 2, $\eta_{lm/um}$ = 30) or lower-viscosity (model 3, $\eta_{lm/um}$ = 1) lower mantle. (c and d) Uncoupled shear zone models (η_{sz}/η_o = 1) with a higher-viscosity (model 5, $\eta_{lm/um}$ = 30) or lower-viscosity (model 6, $\eta_{lm/um}$ = 1) lower mantle. Columns and legend are the same as defined in Figure 5.

the outer rise is locally reduced to $\sim 5 \times 10^{22}$ Pas (Figures 4g and 4h) consistent with estimates from energy dissipation constraints [*Conrad and Hager*, 1999] and plate motion studies [*Buffett and Rowley*, 2006].

[30] In addition to weakening around the slab, the non-Newtonian rheology leads to a slightly larger viscosity jump than is imposed at a depth of 670 km ($\times$20, instead of $\times$10) and a lower average upper mantle viscosity (8×10^{19} Pas) in the region of the subduction zone ($\phi = 25°$) compared to the model boundary ($\phi = 0°$; Figure 4h). The lowest viscosity in the model ($\sim 1 \times 10^{18}$ Pas) occurs in the mantle wedge corner and in response to small-scale instabilities that form at the base of the thickening, overriding-plate lithosphere (Figure 4c). Some of these instabilities are entrained in the slab-induced flow and can travel several hundreds of kilometers into the mantle wedge and down the surface of the slab (see Animation 1).

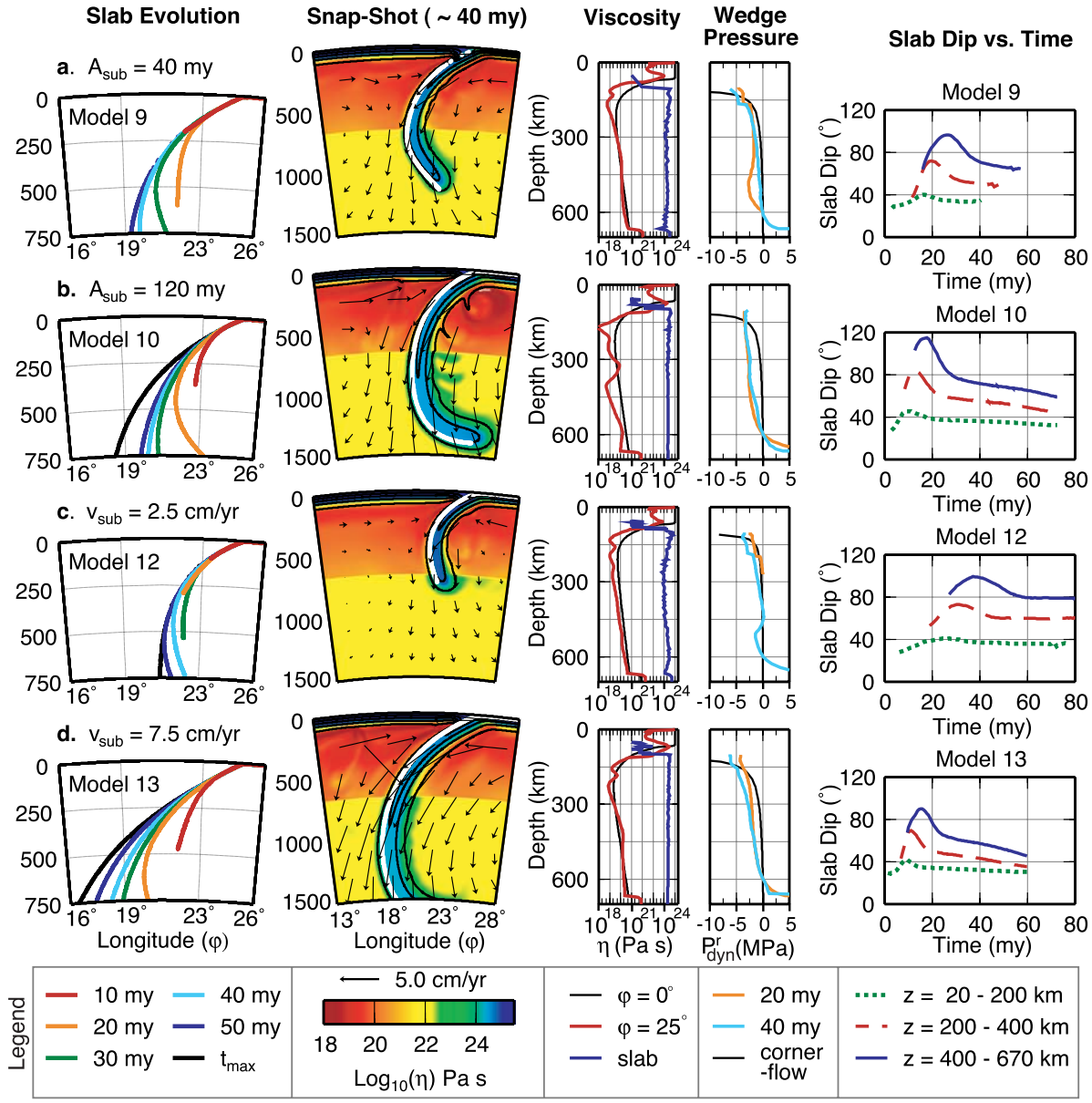

Figure 7. Slab evolution dependence on subduction parameters. (a) Younger subducting plate (model 9, A_{sub} = 40 my). (b) Older subducting plate (model 10, A_{sub} = 120 my). (c) Slower convergence velocity (model 12, v_{sub} = 2.5 cm/yr). (d) Faster convergence velocity (model 13, v_{sub} = 7.5 cm/yr). Columns and legend are the same as defined in Figure 5.

[31] The dynamic pressure, P_{dyn}, is the pressure that develops in response to viscous flow and contributes to normal stresses on the surface of the slab. As in the rigid-slab, corner-flow models of steady-state subduction [e.g., *Stevenson and Turner*, 1977], a region of low dynamic pressure forms above the slab creating a suction force that pulls the slab up. Profiles of dynamic pressure along the surface of the slab are similar to that expected from a corner flow by 35 my, and increase in magnitude and depth extent for later times (Figure 4i). For most of the simulation the suction force on the slab is not sufficient to balance the negative buoyancy of the slab. However, it does help to decrease the slab dip at depths of 100–300 km, in conjunction with the strength of the slab and viscous support of the lower mantle portion of the slab.

4.2. Slab Evolution and Rheology

[32] To investigate how the slab evolution for model 1 depends on mantle rheology, we ran

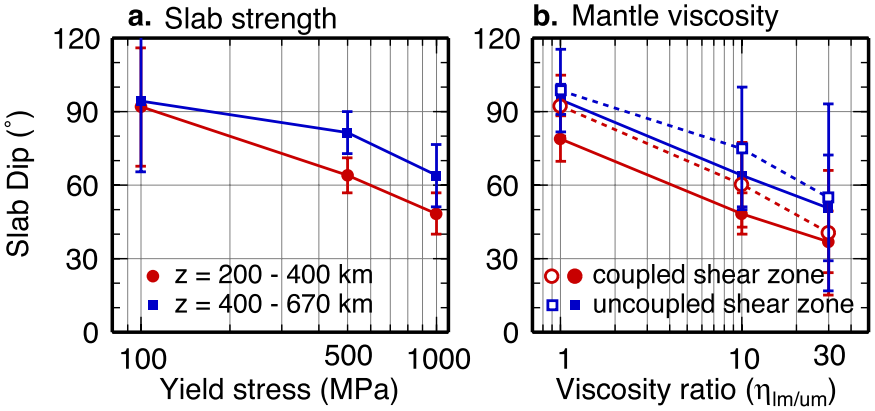

Figure 8. Summary of mantle viscosity structure models. (a) Slap dip decreases with increasing yield stress of the slab and is consistent with observations for σ_y = 1000 MPa. (b) Slab dip decreases for larger upper to lower mantle viscosity jumps, while decreasing shear zone coupling increases slab dip (closed symbols/solid line: slab dip for z = 200–400 km; open symbols/dashed line: slab dip for z = 400–670 km).

models with different slab water content or yield stress, different lower mantle viscosity and different shear zone viscosity.

4.2.1. Slab Strength

[33] The change in dip and shape of the slab with duration of subduction depends on the integrated strength of the slab, which takes into account both the maximum viscosity of the slab and the width of this high-strength region. Figure 2c shows the difference in viscosity profiles across slabs with different water contents. The width of the high-viscosity region (width at half-maximum) for the wet slab is 20–30 km less than the width of the dry slab. This difference in integrated strength changes the long-term evolution of the wet slab (model 1ws), which has steeper dips throughout (Figures 5a and 5b).

[34] The yield stress of the slab also limits the maximum viscosity and integrated strength of the slab. As illustrated in Figures 2c and 4, the yielding portion of the slab in all models lies between the 700°C and 850°C isotherms, depending on the strain rate at these temperatures in the slab. For model 1 with a yield stress of 1000 MPa, the maximum viscosity of the slab is $\sim 5 \times 10^{24}$ Pas over a width of 90 km. This high-viscosity slab supports the weight of the slab and maintains

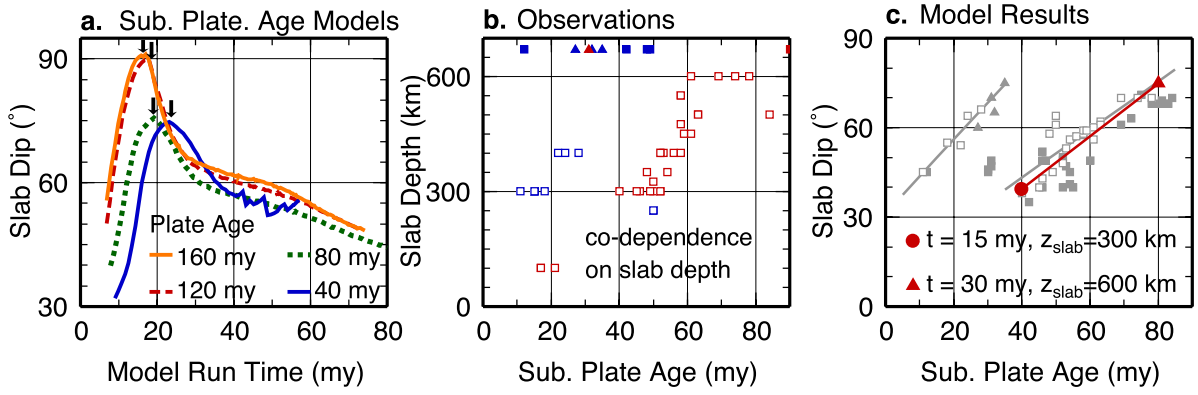

Figure 9. Summary of slab evolution dependence on subducting plate age. (a) Slab dip versus model run times for four models. Slab dip is greater for older slabs and increases with time until the slab enters the lower mantle (black arrows). (b) For upper mantle slabs with retreating, continental, upper plates (open, red squares), there is a correlation between the age of the subducting plate and the maximum slab depth (see text for discussion). (c) Observed slab dip dependence on subducting plate age compared to the model trend for a 40 my slab with a maximum depth of 300 km (red circle) and an 80 my slab with a maximum depth of 600 km (red triangle).

shallow dips throughout the upper mantle (Figure 5a). A slab with an intermediate yield stress (model 7: 500 MPa, $\eta_{slab} \sim 10^{24}$ Pas; Figure 5c) behaves similarly to the stiffer slab, with slightly steeper dips for depths of 200–670 km (10–20° steeper) until it reaches the lower mantle. Upon entering the higher-viscosity lower mantle, the slab thickens to accommodate the difference in viscous resistance between the two layers. Because this slab is not strong enough to transmit stresses up to the upper mantle slab, there is no mechanism to cause the upper mantle portion of the slab to migrate laterally and the slab dip remains at ~80°. However, decreasing the yield stress to 100 MPa (model 8), decreases the maximum slab viscosity to $\sim 10^{22}$ Pas and causes the slab to detach from the subducting plate when it reaches a depth of approximately 300 km (Animation 2). This result is quite different from the vertically sinking and thickening weak slabs found in models that use a viscosity cut-off of 10^{22}–10^{23} Pa s (e.g., 100–1000 × η_o). Therefore the process by which slab strength is limited has a significant effect on the model dynamics.

4.2.2. Mantle Viscosity Structure

[35] Lateral migration of the slab is a direct consequence of the difference in viscous resistance in the upper and lower mantle and the ability of the stiff slab to transmit stress up dip. Models 2 and 3, are identical to model 1 except for the magnitude of the viscosity increase in the lower mantle (Figures 6a and 6b). During the first 20 my of subduction, the slab evolution in the upper mantle is the same in all three models, as seen in the slab shape and dip. However, in model 2 the 30-fold viscosity jump causes the slab to sink more slowly in the lower mantle and to migrate sideways at a faster rate (Animation 3). As more of the slab enters the lower mantle and the viscous resistance increases, the deeper portion of the slab migrates laterally more slowly than the shallower parts of the slab. The difference in lateral migration rates toward the overriding plate produces a slab profile that curves back beneath shallower portions of the slab even though the deeper portion of the slab is sinking vertically.

[36] In contrast, model 3, with no imposed viscosity increase in the lower mantle, exhibits very little lateral migration (~0.1 cm/yr). Instead, the slab sinks near vertically into the lower mantle, while the upper mantle slab maintains a steep, but curved profile (Animation 4). In addition, due to the decrease in viscous support from the lower mantle, the upper mantle portion of the slab must support more weight from the lower mantle portion of the slab. The higher stresses on the upper mantle portion of the slab lead to a reduction in the slab viscosity by about a factor of two to ten.

[37] In models 1 and 2, the slab dip for depths less than 200 km evolves to ~30° (Figures 6a and 6b). The duration of stable subduction, t_{st} (Table 3), is controlled by the rate of lateral migration and the local balance between negative slab buoyancy and flow-induced suction in the wedge corner. For longer durations of subduction, continued lateral migration of the slab could further shallow the slab and cause it to flatten beneath the overriding plate. However, for the time-span of models presented here, of up to 100 my, all the slabs have stable slab dips of greater than 30°.

4.2.3. Plate Boundary Coupling

[38] The shear zone viscosity in models 1–3 is 10 times greater than the upper mantle reference viscosity ($\eta_o = 10^{20}$ Pas), which is a minimum of 10^4 lower than the surrounding lithosphere. This low viscosity maintains the separation between the two plates and minimizes entrainment of the overriding plate by the slab. However, this viscosity also provides a small degree of coupling between the subducting and overriding plates, which helps to unbend the subducting lithosphere as it is forced to follow the shallow dip of the overriding plate. This effect is seen by comparing the slab shapes in models 1–3 to those in models 4–6, in which the shear zone viscosity is a factor of 10 smaller (Figures 6c and 6d and Animations 5 and 6). The initial slab dip in these uncoupled models is steeper (50–90°) and the slab tip curves backward in the upper mantle. This curvature is the result of the stiff slab interior, which maintains the curved shape of the slab that results from bending 30° into the subduction zone.

[39] Once the slab enters the lower mantle, it evolves in the same manner as models with a coupled shear zone, migrating laterally for a 10–30 fold increase in viscosity or sinking vertically for no increase in lower mantle viscosity. In addition, the slightly weaker slab in model 6 unbends more quickly in response to the weight of the slab, while the initial curvature remains for the stiffer slab (model 5) as it sinks through the lower mantle. At shallow depths, the slab dip also steadily decreases to 30–40° for the models with a more viscous lower mantle, but remains at 90° for model 6 with a weaker lower mantle. The slab in

model 6 is slightly weaker than the other slabs because more of the slab weight must be supported by the slab strength in the absence of support from the lower mantle and shear zone coupling. The higher stress within the slab interior causes the slab to yield and the effective viscosity to decrease. Because the slab is slightly weaker in model 6 and there is no migration of the deeper slab to shallower dips, a corner-flow does not develop in the mantle wedge.

4.3. Slab Evolution and Subduction Parameters

[40] We have shown how the viscosity structure affects slab evolution while keeping the subducting plate age and convergence velocity constant; however, these two parameters directly affect the slab temperature, which in turn affects both the slab density and slab viscosity. In addition, as shown in Figure 1, observed slab dip decreases for increasing convergence velocity and shows a linear dependence on plate age for a subset of upper mantle slabs.

[41] The applicability of these simulations to understanding slab dynamics in the Earth can be evaluated by comparing the correlations among the parameters in our models to those observed in nature. In our models, for slabs with ages of 40–160 my, there is almost no difference in the average slab dip at intermediate or deep depths (Figures 7a and 7b and Table 3). Younger slabs do have slightly shallower dips than older slabs before entering the lower mantle ($\sim$5° per 20 my age difference); however, this is a much smaller difference than the observed 30° range in dip for slabs with ages between 40 and 80 my (Figure 1e). We will return to this observation in the discussion. The evolution of the slabs after entering the lower mantle is remarkably similar given the difference in the integrated strength of young and old slabs (Figures 7a and 7b and Animations 7 and 8).

[42] In contrast, there is a clear correlation of slab dip with convergence velocity after the slab enters the lower mantle. In agreement with observations, shallower slab dips develop for faster convergence rates (Figures 7c and 7d and Animations 9 and 10). The initial evolution of slow and fast slabs is similar, indicating that while in the upper mantle, slab dynamics are controlled by a balance between slab strength and buoyancy. However, once the slabs enter the lower mantle, the difference in convergence velocity results in a difference in lateral migration rate. The slowly converging slab quickly reaches steady state at a dip of about 60°, whereas the faster converging slabs migrate laterally with a rate of 1.0 cm/yr at the upper-lower mantle boundary. The decrease in slab dip with time increases the magnitude of the lower-pressure region above the slab, which also helps to decrease the dip of the shallow portions of the slab (Figures 7c and 7d).

5. Discussion

[43] On the basis of the results of the models used to explore the effects of the mantle viscosity structure, we find that slab dip depends strongly on the yield strength of the slab, the viscosity jump into the lower mantle and the shear zone viscosity. Unlike previous models with weak slabs that sink vertically into the mantle without trench motion, these models exhibit non-steady-state behavior and a large range in slab dip. The observed dip of slabs at shallow depths (Figures 1a and 1b) is consistent with a dry slab with yield strength of 1000 MPa, resulting in a maximum slab viscosity of 10^{24}–10^{25} Pas (Figure 8a). Slab dip is also smaller for a higher-viscosity lower mantle, which causes the upper mantle slab to migrate laterally (Figure 8b). Steeply dipping slabs that result from models without an imposed viscosity jump are inconsistent with the observation that slabs without trench motion have a range of slab dips that are less than 90° (Figure 1c). The upper mantle dip of slabs in models with a factor 10–30 viscosity jump are consistent with observations. It is more difficult to evaluate whether the rapid change in slab dip at 670 km in models with the larger viscosity jump are consistent with observed slab shapes because tomographic images of slabs have lower resolution beneath the transition zone. Decreasing the plate boundary coupling leads to steeper slabs (Figure 8b). The observed small dip of slabs at shallow depths (<200 km) is consistent with a small amount of coupling along the plate boundary, which helps to unbend the slab.

5.1. Subducting Plate Age

[44] The time dependence of slab dip for models with different plate ages indicates that the lack of a clear trend for all subduction zones may be due to variations in the strength of the slabs and a change in slab behavior after entering the lower mantle. Two observations support this conclusion. First, there is an increase in slab dip with age before slabs enter the lower mantle (Figure 9a), but this increase is much smaller than the observed trend

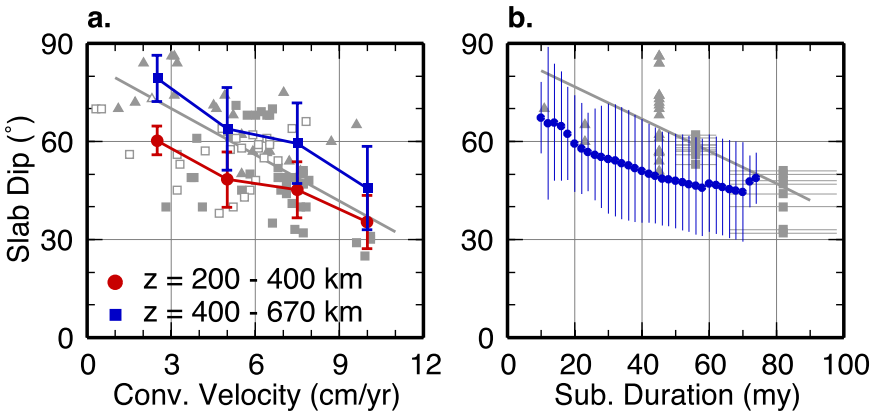

Figure 10. Summary of slab evolution dependence on convergence velocity and subduction duration. (a) Slab dip decreases with increasing convergence velocity, with a trend and magnitudes similar to the observed data (model results for σ_y = 1000 MPa; gray symbols and line fit from Figure 1c). (b) Mean slab dip and standard deviation for models with $\eta_{lm/um}$ = 10, and σ_y = 1000 MPa (1, 4, 9–14). All models show a slow decrease in the upper mantle slab dip (z = 125–670 km) after the slab enters the lower mantle, with a similar slope to that observed, but at smaller dips.

for upper mantle slabs. One possible explanation for the difference in predicted and observed dips is that the observed variation in plate boundary dip by ±9° with plate age is not included in our models. However, the steeper slab dip observed at greater depth varies by more than 30° for slab ages between 40 to 80 my, so plate boundary dip alone is not sufficient to explain the difference between the models and the observations. The weak dependence on slab age in the absence of other complications (e.g., lower mantle support) suggests that the effects of higher integrated slab strength for older slabs is more important than the increase in negative slab buoyancy with age. Second, all the models show that slab dip increases as the slab length increases (i.e., increasing negative slab buoyancy) until the slab reaches the ULM boundary (black arrows in Figure 9a). This change in slab dip with slab length (30° to 75°) is similar to the observed variation in dip of upper mantle slabs with slab age (Figure 1e).

[45] The correlation of slab dip with slab length in the models motivated us to look for this same correlation in the observations. We found that plate age correlates with both the observed maximum slab depth and slab dip for slabs with retreating, continental overriding plates (Figure 9b). In other words, younger slabs are also shorter slabs, which tend to have shallower dips, while older slabs are also longer slabs, which tend to have steeper dips. These results suggest that the observed correlation (Figure 1e) is in fact a function of the maximum slab depth rather than slab age. For example, the trend in the data is well matched in our models if we compare the dip of a 40 my old slab when it has reached 300 km depth and to the dip of an 80 my slab when it has reached 650 km (Figure 9c). The trend for younger slabs beneath advancing overriding plates may have a similar explanation, although there are not enough observations to evaluate this possibility.

5.2. Subduction Velocity and Duration

[46] The correlation between slab dip and convergence velocity in the models with σ_y = 1000 MPa agrees with the observed trend in the data (Figure 10). This result is the same as that predicted by corner-flow models with rigid slabs. However, in the dynamic models the shallower dip for faster slabs results from the combined effects of lateral migration of the slab due to the ULM viscosity jump, and the corner-flow suction at shallower depths and later times (compare corner-flow and model wedge pressure profiles in Figures 7c and 7d). The lateral migration of the slab in the upper mantle also leads to a slow shallowing of the slab with subduction duration that agrees with the trend in observations. No effort was made to *tune* these models to observations, as the choice of rheology was motivated by laboratory constraints. The good agreement between models and results for both the dip trends and magnitudes suggests that using a realistic rheologic model based on laboratory constraints is essential for studying the dynamics of subduction.

[47] The importance of flow-induced stresses (mantle wedge flow) on slab dynamics is also

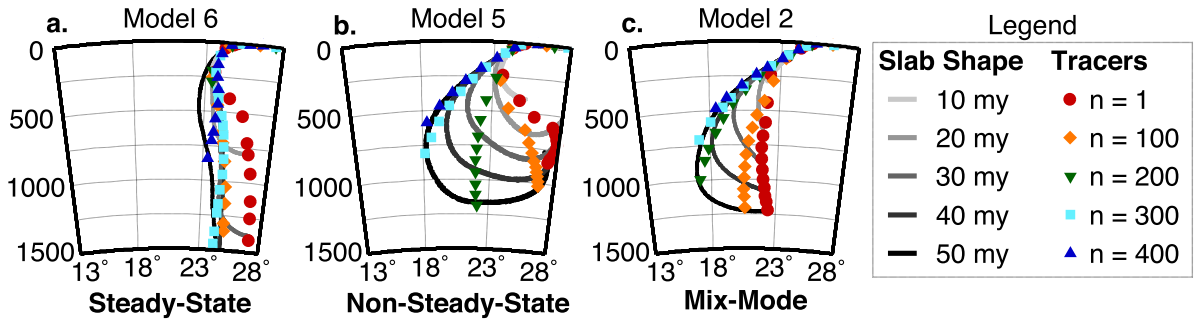

Figure 11. Illustration of steady-state, non-steady-state, and mix-mode slab evolution. Location of tracer particles (symbols) shows flow path of slab material through the mantle as function of time, while slab shape profiles (gray-scale profiles) show the location of slab material at a fixed time (see legend). (a) Steady-state subduction: slab shape and tracer particle paths are the same. (b) Non-steady-state subduction: slab shape profiles do not match tracer particle paths. A snapshot of slab shape does not represent the path material has flowed. (c) Mix-mode subduction: slab shape and tracer particle paths agree for initial and final stages, interrupted by an episode of slab migration.

consistent with the observed increase in slab dip with increasing motion of the upper plate away from the subducting plate (Figure 1c) [*Lallemand et al.*, 2005]. Viewed from the reference frame of a fixed trench, motion of the upper plate away from the subducting plate acts to reduce the magnitude of flow velocities in the mantle wedge, which reduces the suction force on the slab. Better correlations among subduction parameters for slabs that have crossed into the lower mantle is also consistent with the stabilizing effect of the higher-viscosity lower mantle on slab dynamics, which dominates over other processes. Significant viscous support of the lower mantle slab also agrees with previous results that found an improved fit to global plate motions for models in which the lower mantle slab contributes little to the slab force pulling the plates [*Conrad and Lithgow-Bertelloni*, 2002].

5.3. Modes of Slab Evolution

[48] Observations of seismicity and tomographic images provide snapshots of the shapes of slabs and are often interpreted as the path the material took into the mantle. This type of comparison can be deceiving if the evolution of the slab is not steady state. The difference between the slab shape, defined by the position of all tracer particles at a particular time, and the flow path of slab material, tracked by the location of a single tracer at a series of times, depends on the time dependence of slab evolution. If the slab shape does not change (steady-state), then slab shape is a good indication of the flow path (Figure 11a). However, if the slab shape changes either continuously (non-steady-state) or episodically (mix-mode), as it does when the upper mantle slab migrates laterally, then the slab shape and flow paths can differ significantly (Figures 11b and 11c and Table 3). In all of these models, the material paths through the lower mantle are dominated by vertical sinking, while the flow paths in the upper mantle depend on the slab strength and mantle viscosity structure. For example, if only the final snapshot of the slab shape in model 5 was known and interpreted as a flow path, one would infer that there is considerable lateral flow in the mid-mantle, while in fact the flow in the mid-mantle is primarily vertical. The time dependence of slab behavior illustrates how using the present-day shapes of slabs could lead to incorrect conclusions about the pattern of mantle flow.

5.4. Other Factors Affecting Slab Dynamics

[49] Several factors that affect slab dynamics have not been considered in our models including the effects of phase changes at 410 km and 670 km, localized reductions in viscosity due to grain-size variations in the slab, or water and melt in the mantle wedge, and trench migration. We consider how some of these factors might affect slab evolution, based on previous results and the dependence of slab dynamics on rheology observed in our models:

[50] 1. Changes in slab buoyancy due to phase transitions could lead to steepening of the slab at 410 km (olivine-spinel) while decreasing the slab descent rate and increasing lateral migration at 670 km (spinel-perovskite). In particular, the added resistance due to the phase transition at 670 km depth would have an effect similar to a larger viscosity jump, in which case models with a lower intrinsic viscosity (e.g., models 3 and 6) could result in more shallow-dipping slabs. However, on the basis of previous models using similar

rheology [*Cížková et al.*, 2002], we do not expect the spinel-perovskite phase change to prevent the slab from sinking into the lower mantle.

[51] 2. Any slab weakening mechanism, such as grain-size reduction accompanying a phase change [*Rubie*, 1984; *Riedel and Karato*, 1997] or warming of the slab due to latent heat effects [*van Hunen et al.*, 2001] would lead to steeper slabs that sink directly into the lower mantle, if there is no lateral migration in the upper mantle, similar to our models with a lower yield stress.

[52] 3. Localized regions of low viscosity caused by high water or melt content in the mantle wedge could allow the hot mantle to advect to shallower depths and thereby decrease the length of the coupled plate boundary [*Kelemen et al.*, 2003], or could decrease the magnitude of the dynamic pressure in the wedge corner [*Billen et al.*, 2003]. Both effects would lead to steeper slab dips.

[53] Finally, trench migration is clearly an important factor in several subductions zones, and may be the dominant control on slab dynamics for slabs of short lateral extent, where toroidal flow around the edge of the slab has a strong influence on slab dynamics [*Funiciello et al.*, 2006; *Stegman et al.*, 2006; *Royden and Husson*, 2006; *Schellart et al.*, 2007]. Small slab dips at early stages of subduction are also likely to be controlled by slab roll-back [*Gurnis et al.*, 2004]. However, *Karato et al.* [2001] suggest that the rate and direction of trench migration may depend on variations in slab strength and therefore may be a result of slab dynamics rather than a cause. The agreement between our model predictions and the global data set of slab profiles away from slab edges shows that slab strength and mantle viscosity structure have a dominant influence on the long-term behavior of slabs. Therefore trench migration, which may vary in rate, over space and over time, likely modifies the long-term behavior of slabs in the upper mantle, by playing a primary role over short intervals of time, for example, during subduction initiation or periods of plate reorganization.

5.5. Conflicting Constraints on Slab Strength

[54] Our models employ a mantle and slab rheology constrained by laboratory experiments resulting in slab dynamics that are consistent with observations. In particular, the dislocation creep mechanism (non-Newtonian viscosity) plays a key role by reducing the viscosity around the slab, allowing it to easily subduct through the upper mantle and to migrate laterally, and by reducing the mantle wedge viscosity, which keeps the subducting plate and overriding plate decoupled [*Billen and Hirth*, 2005]. The high yield strength (1000 MPa) or high viscous strength of the slab (10^{24}–10^{25} Pas) is also required to reproduce the observed range in slab shape, the shallow slab dips, the decrease in slab dip with time, and the small dependence on plate age. Although the slabs in our models are relatively strong, strain rates in the slabs are consistent with that expected from seismic moment release [*Bevis*, 1988], and weakening within the shallow subduction zone is consistent with estimates from several other approaches [*Conrad and Hager*, 1999; *Billen and Gurnis*, 2005; *Buffett and Rowley*, 2006]. In addition, recent research on subduction initiation that includes similarly strong lithosphere indicates that initiation can occur with reasonable plate forces [*Hall et al.*, 2003; *Gurnis et al.*, 2004].

[55] However, this high viscous strength appears to be at odds with some previous estimates of slab strength from regional and global geoid models, the orientation of stress axes in the slab, and the earthquake-depth distribution in slabs, as discussed in the introduction. All of these previous models have one aspect in common, which may provide a way of reconciling these results: they all assume that the slab and lithosphere have one uniform and continuous viscosity that is not stress-dependent. However, the yield stress included in our models naturally leads to variations in strength along the slab and within the hinge zone of the subducting plate near the surface.

[56] These lateral variations in viscosity within the slab change the way in which the slab transmits stresses and couples to the subducting and overriding plate. For example, using instantaneous models of the Tonga-Kermadec subduction zone *Billen et al.* [2003] concluded that a weak slab was necessary to match the magnitude of dynamic topography in the fore-bulge of the subducting plate and island arc region of the overriding plate. These regions of the surface topography are strongly dependent on the coupling between the slab and the subducting plate, which is controlled by the slab strength at shallow depths. However, the Tonga-Kermadec models used Newtonian rheology and did not explore the consequences of a weak hinge zone within an otherwise stiff slab. While it is not obvious how including a stress-dependent slab rheology would change the results in each of

these other studies, it is known that lateral variations in viscosity can lead to significant changes in the geoid and dynamic topography by changing the coupling between different components of the subduction system [*Zhong and Davies*, 1999; *Billen and Gurnis*, 2001]. Further studies are needed to determine if these other observations can also be well-matched by stronger slabs with yielding that leads to localized weak regions within the slab.

6. Conclusions

[57] This study demonstrates how several processes affect slab dynamics in the absence of trench migration and provides a framework in which to interpret other subduction observations. We have shown that the observed geometry of slabs and several correlations among subduction observations (away from slab edges) are well-matched by models including dry slabs with a yield stress of 1000 MPa, a factor of 10 jump in viscosity into the lower mantle, and a small degree of coupling along the plate boundary. Our models reproduce the observed decrease in slab dip with increasing convergence velocity and duration of subduction. We find only a small direct dependence of slab dip on plate age while slabs are in the upper mantle. However, combined with the increase in slab dip with slab length, we are able to match an apparent correlation between slab dip and slab age for young upper mantle slabs with retreating, continental overriding plates.

[58] We find that the main processes controlling slab evolution are as follows:

[59] 1. Non-Newtonian rheology in the upper mantle decreases viscous resistance around the slab allowing it to deform more freely in the upper mantle, while the stiffer, Newtonian lower mantle provides a stabilizing effect on slab evolution.

[60] 2. In the absence of trench migration, slab evolution in the upper mantle is characterized by initially shallow slab dips that increase as the slab lengthens in the upper mantle.

[61] 3. Slab dip in the upper mantle decreases after strong slabs enter a higher-viscosity lower mantle and begin to migrate laterally.

[62] 4. Slab dip decreases with increasing convergence velocity for stiff slabs that enter the lower mantle as a result of lateral migration of the slab at the ULM boundary and to a lesser extent on flow-induced suction in the wedge corner.

[63] 5. Slab dip does not directly correlate with slab buoyancy, because the slab stiffness has a stronger affect on dynamics than small differences in slab density due plate age.

[64] 6. Slab evolution is not steady state, and caution should be used in interpreting slab shapes as flow paths through the mantle.

[65] On the basis of these results we conclude that, in the absence of trench motion, slab strength and the difference between upper and lower mantle viscosity play the primary role in determining the long-term evolution of slabs, while corner-flow in the mantle wedge affects the dip of the shallow slab and duration of stable subduction.

Appendix A

[66] The choice of boundary conditions is particularly important in modeling the time-dependent nature of slab dynamics. Because the boundary conditions always influence flow within the model domain, it is essential to clearly understand the influence of the boundary conditions on the slab dynamics and to minimize these effects where possible.

A1. Reflecting Side-Walls

[67] We explicitly create a reference frame for motion that is fixed with respect to the model domain by choosing reflecting boundary conditions for our models. Thus we can study slab evolution in the absence of trench motion. By contrast, in models with periodic boundary conditions, flow out of one boundary comes back into the model domain at the other boundary, implicitly creating a reference frame that is relative to the net motion of the lower mantle (which usually moves in the direction of subduction). As a result, there will be relative motion (slab rollback) between the trench and flow in the deep mantle, even if the trench is held fixed with respect to the model domain [*Gurnis and Hager*, 1988; *Han and Gurnis*, 1999; *Enns et al.*, 2005].

[68] However, reflecting boundary conditions can also affect slab dynamics [*Han and Gurnis*, 1999; *Enns et al.*, 2005]. In particular they can cause weak slabs to curl back under the subducting plate. Indeed, in our earlier models in which the depth of the model domain only extended to 1500 km, we found that even strong slabs curl backward, regardless of the width of the model domain. This led us to conclude that the slabs curled backward,

not because the domain width was too small, but because the return flow is confined to a shallow layer. By confining the flow to a shallow layer, there is a strong lateral flow component that pulls the slab backward underneath the subducting plate. By increasing the depth of the model domain to the core-mantle-boundary, neither weak nor strong slabs curl backward. Instead, weak slabs sink vertically into the mantle and strong slabs migrate under the overriding plate. These models still include a return flow to the side-walls, but because material is free to flow up from the lower mantle, rather than having to flow laterally from the subduction zone, flow throughout the upper mantle is directed toward the subduction zone.

A2. Work Done by Kinematic Surface Boundary Condition

[69] In previous studies, prescribed surface velocity boundary conditions have been used in a variety of ways to control where subduction occurs, the rate of subduction and trench migration [e.g., *Christensen*, 1996; *Kincaid and Sacks*, 1997; *Cížková et al.*, 2002]. Models that are driven only by slab buoyancy are preferred for their inherent realism [e.g., *Enns et al.*, 2005]. However, when the effect of surface boundary conditions on the evolution of the slab is minimal, these boundary conditions provide a method to control specific parameters of interest (e.g., subduction velocity, subducting plate age).

[70] The influence of kinematic boundary conditions on the mantle flow is assessed by determining the amount of work done by the boundary conditions on the subducting plate and comparing this to the work done by the subducting plate and the slab on the mantle. If the work done by the surface boundary conditions is dissipated within the lithosphere near the top surface of the subducting plate, then this energy is not available to drive flow in the mantle. In addition, if the work done by the slab on the mantle is greater than the work done by the subducting plate, then this shows that the sinking of the slab is driving the flow in the mantle.

[71] It has been shown for weak to moderately stiff lithosphere that the work done by kinematic boundary conditions on the surface of the subducting plate is largely dissipated within the lithosphere and does not drive flow or influence slab dynamics in the mantle [*Han and Gurnis*, 1999]. However, the amount of work done by the kinematic boundary condition and the dissipation of energy within the lithosphere depends on the rheology. Because the rheology used in our models leads to more viscous slabs (1000 times higher viscosity than previous models), we repeat the work assessment here to determine the effect of the boundary conditions on the slab evolution in our models.

[72] We calculate the work done, per unit length of trench, along isotherms within the subducting plate and along the surface of the slab (defined as the $T = 700^{\circ}$C isotherm),

$$W = \delta\tau \int_o^L \sigma_{nt} v_t \partial l \tag{A1}$$

where σ_{nt} and v_t are the shear stress and tangential velocity, respectively, on the isotherm surface of length, L, with a surface-normal direction, **n**, and tangent direction, **t**, and $\delta\tau$ is a constant increment of time (the time-step in the models is approximately 10,000 years). Initially the work done by the plate exceeds the work done by the slab in agreement with subduction initiation models [*Hall et al.*, 2003]. However, once the down-dip length of the slab is 100–200 km long (10–20 my after the start of the model) the work done by the slab, W_{slab}, grows to 50 to 300 times larger than the work done by the plate, W_{plate} (along the top surface) on the underlying mantle (Figures A1a–A1c). For most of the evolution of the slabs, the work done by the boundary condition is less than 2–4% of the work done by the slab.

[73] The work done by the velocity boundary condition is dissipated in two locations in the subducting plate. First, the work introduced by the boundary condition is rapidly dissipated near the depth of the 600–900°C isotherms and therefore cannot drive flow in the mantle (Figures A1d–A1f). The rapid drop in work occurs at the transition from deformation by plastic yielding to viscous flow, where the combined effects of temperature- and stress-dependent rheology lead to a strong decrease in viscosity. The magnitude of the work done in the plate and slab increases for higher velocities and older plates, and also increases slightly for models with a coupled shear zone or higher-viscosity mantle.

[74] Second, for all models, it is observed that the magnitude of velocity within the subducting plate decreases to 70–90% of the applied velocity where the plate turns to subduct parallel to the shear zone. A low-viscosity region develops, marking the location where the work within the shallow portion

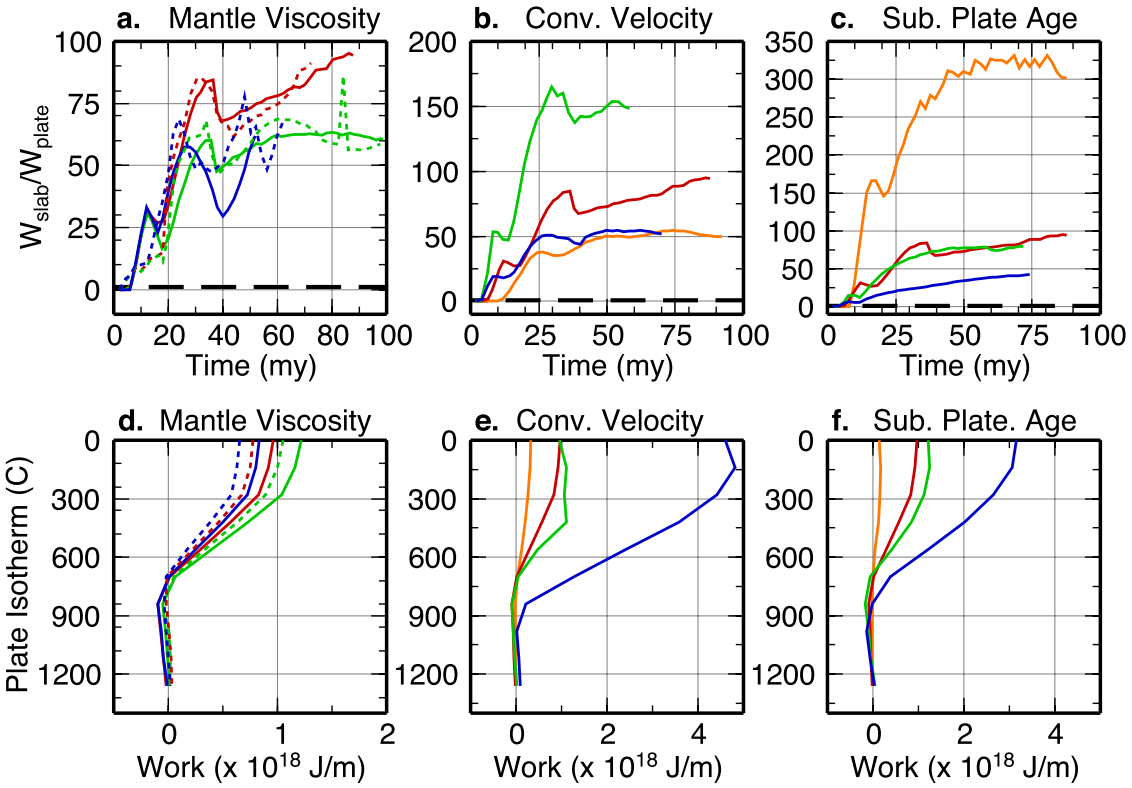

Figure A1. Work done by kinematic boundary conditions. (a–c) Ratio of work done by the slab ($T = 700°$ contour) to work done by the plate (at the surface). (a) Mantle viscosity structure models (solid: models 1, red; 2, green; 3, blue; dashed: models 4, red; 5, green; 6, blue). (b) Convergence velocity models (1, red; 12, orange; 13, green, 14, blue). (c) Subducting plate age models (1, red; 9, orange; 10, green; 11, blue). Work done by the slab is larger than work done by the plate in all models for times >10 my. (d–f) Median work done by the plate, for all times, along isotherms (proxy for depth) in the plate. Panels and curves are the same as in Figures A1a–A1c. Note that the large work ratio for model 9 ($A_{sub} = 40$ my) is due to the shorter plate length relative to model with older subducting plate, but the work done by the slab is comparable in all models.

of subducting plate is dissipated (Figure 4g). Beyond this point the slab velocities are almost constant throughout the upper mantle indicating that the slab is not significantly shortening or stretching. These results show that the work done by the kinematic boundary condition is dissipated within the subducting plate and does not affect the flow in the underlying mantle or the dynamics of the slab.

Acknowledgments

[75] This research was partially supported by NSF award EAR0125919. We thank Jeroen van Hunen and an anonymous reviewer for constructive reviews, which pointed out several important points that were added to the introduction and discussion.

References

Arcay, D., E. Tric, and M.-P. Doin (2007), Slab surface temperature in subduction zones: Influence of the interplate decoupling depth and upper plate thinning processes, *Earth Planet. Sci. Lett.*, *255*, 324–338.

Bellahsen, N., C. Faccenna, and F. Funiciello (2005), Dynamics of subduction and plate motion in laboratory experiments: Insights into the "plate tectonics" behavior of the Earth, *J. Geophys. Res.*, *110*, B01401, doi:10.1029/2004JB002999.

Bevis, M. (1988), Seismic slip and down-dip strain rates in Wadati-Benioff Zones, *Science*, *240*, 1317–1319.

Billen, M. I., and M. Gurnis (2001), A low viscosity wedge in subduction zones, *Earth Planet. Sci. Lett.*, *193*, 227–236.

Billen, M. I., and M. Gurnis (2005), Constraints on subducting plate strength within the Kermadec trench, *J. Geophys. Res.*, *110*, B05407, doi:10.1029/2004JB003308.

Billen, M. I., and G. Hirth (2005), Newtonian versus non-Newtonian upper mantle viscosity: Implications for subduction initiation, *Geophys. Res. Lett.*, *32*, L19304, doi:10.1029/2005GL023457.

Billen, M. I., M. Gurnis, and M. Simons (2003), Multiscale dynamic models of the Tonga-Kermadec subduction zone, *Geophys. J. Int.*, *153*, 359–388.

Braun, M. G., G. Hirth, and E. M. Parmentier (2000), The effects of deep damp melting on mantle flow and melt generation beneath mid-ocean ridges, *Earth Planet. Sci. Lett.*, *176*, 339–356.

Buffett, B. A., and D. R. Rowley (2006), Plate bending at subduction zones: Consequences for the direction of plate motions, *Earth Planet. Sci. Lett.*, *245*, 359–364.

Christensen, U. R. (1996), The influence of trench migration on slab penetration into the lower mantle, *Earth Planet. Sci. Lett.*, *140*, 27–39.

Cížková, H., J. van Hunen, A. P. van den Berg, and N. J. Vlaar (2002), The influence of rheological weakening and yield stress on the interaction of slabs with the 670 km discontinuity, *Earth Planet. Sci. Letters*, *199*, 447–457.

Conrad, C. P., and B. H. Hager (1999), Effects of plate bending and fault strength at subduction zones on plate dynamics, *J. Geophys. Res.*, *104*, 17,551–17,571.

Conrad, C. P., and C. Lithgow-Bertelloni (2002), How mantle slabs drive plate tectonics, *Science*, *298*, 207–209.

Cruciani, C., E. Carminati, and C. Doglioni (2005), Slab dip vs. lithosphere age: No direct function, *Earth Planet. Sci. Lett.*, *238*, 298–310.

Enns, A., T. W. Becker, and H. Schmeling (2005), The dynamics of subduction and trench migration for viscosity stratification, *Geophys. J. Int.*, *160*, 755–761.

Fukao, Y., S. Widiyantoro, and M. Obayashi (2001), Stagnant slabs in the upper and lower mantle transition zone, *Rev. Geophys.*, *39*(3), 291–323.

Funiciello, F., C. Faccenna, D. Giardini, and K. Regenauer-Lieb (2003), Dynamics of retreating slabs: 2. Insights from three-dimensional laboratory experiments, *J. Geophys. Res.*, *108*(B4), 2207, doi:10.1029/2001JB000896.

Funiciello, F., M. Moroni, C. Piromallo, C. Faccenna, A. Cenedese, and H. A. Bui (2006), Mapping mantle flow during retreating subduction: Laboratory models analyzed by feature tracking, *J. Geophys. Res.*, *111*, B03402, doi:10.1029/2005JB003792.

Garfunkel, Z., C. A. Anderson, and G. Schubert (1986), Mantle circulation and the lateral migration of subducted slabs, *J. Geophys. Res.*, *91*(B7), 7205–7223.

Goetze, C., and B. Evans (1979), Stress and temperature in the bending lithosphere as constrained by experimental rock mechanics, *Geophys. J. R. Astron. Soc.*, *59*, 463–478.

Gudmundsson, O., and M. Sambridge (1998), A regionalized upper mantle (RUM) seismic model, *J. Geophys. Res.*, *103*(B4), 7121–7136.

Gurnis, M., and B. H. Hager (1988), Controls of the structure of subducted slabs, *Nature*, *335*(22), 317–321.

Gurnis, M., C. Hall, and L. Lavier (2004), Evolving force balance during incipient subduction, *Geochem. Geophys. Geosyst.*, *5*, Q07001, doi:10.1029/2003GC000681.

Hager, B. H. (1984), Subducted slabs and the geoid: Constraints on mantle rheology and flow, *J. Geophys. Res.*, *89*(B7), 6003–6015.

Hager, B. H. (1991), Mantle viscosity: A comparison of models from postglacial rebound and from the geoid, plate driving forces, and advected heat flux, in *NATO Advanced Research Workshop on Glacial Isostasy, Sea-Level, and Mantle Rheology, Erice, Italy, July 27–Aug. 4, 1990*, *NATO ASI Ser., Ser. C*, vol. 334, edited by E. B. R. Sabodini and K. Lambeck, pp. 493–513, Springer, New York.

Hall, C. E., M. Gurnis, M. Sdrolias, L. Lavier, and R. D. Müller (2003), Catastrophic initiation of subduction following forced convergence across fracture zones, *Earth Planet. Sci. Lett.*, *212*, 15–30.

Han, L., and M. Gurnis (1999), How valid are dynamic models of subduction and convection when plate motions are prescribed?, *Phys. Earth Planet. Inter.*, *110*, 235–246.

Hirth, G. (2003), Laboratory constraints on the rheology of the upper mantle, in *Plastic Deformation of Minerals and Rocks*, *Rev. Mineral. Geochem.*, vol. 51, edited by S.-I. Karato and H-.R. Wenk, pp. 97–116, Mineral. Soc. of Am., Washington, D. C.

Hirth, G., and D. Kohlstedt (2003), Rheology of the upper mantle and the mantle wedge: A view from the experimentalists, in *Inside the Subduction Factory*, *Geophys. Monogr. Ser.*, vol. 138, edited by J. Eiler, pp. 83–105, AGU, Washington, D. C.

Isacks, B. L., and M. Barazangi (1977), Geometry of Benioff zones: Lateral segmentation and downwards bending of the subducted lithosphere, in *Island Arc, Deep Sea Trenches and Back-Arc Basins, Maurice Ewing Series*, vol. 1, edited by M. Talwani and W. C. Pitman, AGU, Washington, D. C.

Jarrard, R. D. (1986), Relations among subduction parameters, *Rev. Geophys.*, *24*, 217–284.

Kárason, H., and R. D. van der Hilst (2001), Tomographic imaging of the lowermost mantle with differential times of refracted and diffracted core phases (*PKP*, P_{diff}), *J. Geophys. Res.*, *106*(B4), 6569–6588.

Karato, S., and H. Jung (2003), Effects of pressure on high-temperature dislocation creep in olivine, *Philos. Mag.*, *83*(3), 401–414.

Karato, S., and P. Wu (1993), Rheology of the upper mantle: A synthesis, *Science*, *260*, 771–778.

Karato, S.-I., M. R. Riedel, and D. A. Yuen (2001), Rheological structure and deformation of subducted slabs in the mantle transition zone: Implications for mantle circulation and deep earthquakes, *Phys. Earth Planet. Inter.*, *127*, 83–108.

Kelemen, P. B., J. L. Rilling, E. M. Parmentier, L. Mehl, and B. R. Hacker (2003), Thermal structure due to solid-state flow in the mantle wedge beneath arcs, in *Inside the Subduction Factory*, *Geophys. Monogr. Ser.*, vol. 138, edited by J. Eiler, pp. 293–311, AGU, Washington, D. C.

Kemp, D. V. (1992), A model for the subduction mechanics of flexible lithosphere and its viscous coupling to the mantle using power-law rheologies, Ph.D. thesis, Univ. of Calif., Los Angeles.

Kendall, J. M. (2000), Seismic anisotropy in boundary layers of the mantle, in *Earth's Deep Interior: Mineral Physics and Tomography From the Atomic to the Global Scale*, *Geophys. Monogr. Ser.*, vol. 117, edited by S. Karato et al., pp. 133–159, AGU, Washington, D. C.

Kincaid, C., and I. S. Sacks (1997), Thermal and dynamical evolution of the upper mantle in subduction zones, *J. Geophys. Res.*, *102*, 12,295–12,315.

King, S. D. (2001), Subduction zones: Observations and geodynamic models, *Phys. Earth Planet. Inter.*, *127*, 9–24, 2001.

Kohlstedt, D. L., B. Evans, and S. J. Mackwell (1995), Strength of the lithosphere: Constraints imposed by laboratory experiments, *J. Geophys. Res.*, *100*, 17,587–17,602.

Kukaèka, M., and C. Matyska (2004), Influence of the zone of weakness on dip angle and shear heating of subducted slabs, *Phys. Earth Planet. Inter.*, *141*, 243–252.

Lallemand, S., A. Heuret, and D. Boutelier (2005), On the relationships between slab dip, back-arc stress, upper plate absolute motion, and crustal nature in subduction zones, *Geochem. Geophys. Geosyst.*, *6*, Q09006, doi:10.1029/2005GC000917.

McKenzie, D. P. (1969), Speculations on the consequences and causes of plate motions, *Geophys. J. R. Astron. Soc.*, *18*, 1–32.

Moresi, L., and M. Gurnis (1996), Constraints on the lateral strength of slabs from three-dimensional dynamic flow models, *Earth Planet. Sci. Lett.*, *138*, 15–28.

Piromallo, C., T. W. Becker, F. Funiciello, and C. Faccenna (2006), Three-dimensional instantaneous mantle flow induced by subduction, *Geophys. Res. Lett.*, *33*, L08304, doi:10.1029/2005GL025390.

Ricard, Y., C. Doglioni, and R. Sabadini (1991), Differential rotation between lithosphere and mantle: A consequence of lateral mantle viscosity variations, *J. Geophys. Res.*, *96*, 8407–8415.

Riedel, M. R., and S.-I. Karato (1997), Grain-size evolution in subducted oceanic lithosphere associated with the olivine-spinel transformation and its effects on rheology, *Earth Planet. Sci. Lett.*, *148*, 27–43.

Ritsema, J. (2000), Evidence for shear velocity anisotropy in the lowermost mantle beneath the Indian Ocean, *Geophys. Res. Lett.*, *27*, 1041–1044.

Royden, L. H., and L. Husson (2006), Trench motion, slab geometry and viscous stresses in subduction systems, *Geophys. J. Int.*, *167*, 881–905.

Rubie, D. C. (1984), The olivine → spinel transformation and the rheology of subducting lithosphere, *Nature*, *308*, 505–508.

Schellart, W. P., J. Freeman, D. R. Stegman, L. Moresi, and D. May (2007), Evolution and diversity of subduction zones controlled by slab width, *Nature*, *446*, 308–311, doi:10.1038/nature05615.

Schmeling, H., R. Monz, and D. C. Rubie (1999), The influence of olivine metastability on the dynamics of subduction, *Earth Planet. Sci. Lett.*, *165*, 55–66.

Stegman, D. R., J. Freeman, W. P. Schellart, L. Moresi, and D. May (2006), Influence of trench width on subduction hinge retreat rates in 3-D models of slab rollback, *Geochem. Geophys. Geosyst.*, *7*, Q03012, doi:10.1029/2005GC001056.

Stevenson, D. J., and J. S. Turner (1977), Angle of subduction, *Nature*, *270*, 334–336.

Tao, W. C., and R. J. O'Connell (1993), Deformation of a weak subducted slab and variation of seismicity with depth, *Nature*, *361*, 626–628.

Tetzlaff, M., and H. Schmeling (2000), The influence of olivine metastability on deep subduction of oceanic lithosphere, *Phys. Earth Planet. Inter.*, *120*, 29–38.

Toth, J., and M. Gurnis (1998), Dynamics of subduction initiation at preexisting fault zones, *J. Geophys. Res.*, *103*(B8), 18,053–18,067.

Tovish, A., G. Schubert, and B. P. Luyendyk (1978), Mantle flow pressure and the angle of subduction: Non-Newtonian corner flows, *J. Geophys. Res.*, *83*, 5892–5898.

van den Berg, A. P., P. E. van Keken, and D. A. Yuen (1993), The effects of a composite non-Newtonian and Newtonian rheology on mantle convection, *Geophys. J. Int.*, *115*, 62–78.

van Hunen, J., A. P. van den Berg, and N. J. Vlaar (2000), A thermo-mechanical model of horizontal subduction below an overriding plate, *Earth Planet. Sci. Lett.*, *182*, 157–169.

van Hunen, J., A. P. van den Berg, and N. J. Vlaar (2001), Latent heat effects of the major mantle phase transitions on low-angle subduction, *Earth Planet. Sci. Lett.*, *190*, 125–1351.

Vassiliou, M. S., B. H. Hager, and A. Raefsky (1984), The distribution of earthquakes with depth and stress in subducting slabs, *J. Geodyn.*, *1*, 11–28.

Zhong, S., and G. F. Davies (1999), Effects of plate and slab viscosities on the geoid, *Earth Planet. Sci. Lett.*, *170*, 487–496.

Zhong, S., and M. Gurnis (1986), Interaction of weak faults and non-Newtonian rheology produces plate tectonics in a 3-D model of mantle flow, *Nature*, *383*, 245–247.

Zhong, S., M. Gurnis, and L. Moresi (1998), Role of faults, nonlinear rheology, and viscosity structure in generating plates from instantaneous mantle flow models, *J. of Geophys. Res.*, *103*(B7), 15,255–15,268.